# Development of Pure Iron L-PBF Parameters for Biomedical Applications

*José Pedro Pais Pereira*

**Dissertação de Mestrado**

Orientador na FEUP: Prof Jorge Lino Alves

Orientador no INEGI: Pedro Lopes

U.PORTO
FEUP FACULDADE DE ENGENHARIA
UNIVERSIDADE DO PORTO

**Mestrado Integrado em Engenharia Mecânica**

2025-02-24

# Resumo

A tecnologia de Fabrico Aditivo (FA), também conhecida como Impressão 3D, tem revolucionado a engenharia médica, particularmente na fabricação de scaffolds - estruturas tridimensionais que oferecem suporte temporário para o crescimento e regeneração do novo tecido ósseo. Essas estruturas são altamente personalizáveis e possuem alta aderência anatómica, possibilitando uma integração mais eficaz com o organismo. Em geral, os scaffolds apresentam uma estrutura celular, formada por poros e canais que facilitam a penetração de células e tecidos na sua estrutura. Contudo, devido à complexidade geométrica desses componentes, estabelecer parâmetros de fabricação ideais torna-se uma tarefa árdua e demorada. Além disso, as propriedades mecânicas destes materiais em função dos parâmetros de impressão e design ainda não estão completamente compreendidas. Esta dissertação de mestrado procurou contribuir para colmatar as lacunas de conhecimento nestas áreas de estudo. Este trabalho enquadra-se no seguimento de um projeto anterior de maior escala, no qual se efetuaram experiências a nível de design das peças e estudo das suas propriedades mecânicas em função dos parâmetros elegidos. Portanto, esta dissertação surge na continuação desse projeto, no qual as informações obtidas das impressões 3D realizadas anteriormente, servem como ponto de partida. Experimentalmente, iniciou-se uma nova impressão 3D, pelo método de fusão de leito de pó a laser, com uma geometria diferenciada, do qual fazem parte 144 peças, todas elas originadas por parâmetros de impressão diferentes. Este trabalho divide-se em duas tarefas principais: (i) análise do pó utilizado na impressão; (ii) análise das peças impressas. Na primeira fase procedeu-se à análise da dimensão e morfologia das partículas do pó pelos métodos de DLS e SEM, respetivamente. Na segunda etapa do trabalho, as peças impressas foram o alvo de estudo, no qual se efetuou: (i) medição da porosidade; (ii) medição da dureza; (iii) análise da microestrutura; (iv) análise da precisão dimensional do furo interior; e medição/análise da rugosidade. De notar que estas análises tiveram sempre como objetivo associar a influência direta que os parâmetros de impressão têm nas propriedades mecânicas e características na geometria das peças. Os resultados mostraram exatamente isso, que existe uma relação direta entre ambos os fatores. A análise do pó revelou um material com partículas bastante irregulares e de tamanho quase três vezes superior ao anunciado pelo fabricante. Os testes de porosidade revelaram que os melhores resultados correspondem às peças com densidades de energia compreendidas entre 51-54 e 58-63 J/mm$^3$. Enquanto que para a dureza, o intervalo ótimo está compreendido entre 45-59 J/mm$^3$. Para ambas, o parâmetro velocidade de impressão foi o mais determinante, com os melhores resultados a surgirem para 600-800 mm/s. Sendo que porosidade e dureza são as características mais importantes a ter em consideração para alcançar os implantes ósseos desejados, requerendo peças o mais densas possíveis e de dureza considerável, poderá concluir-se desde já que a janela ótima de resultados corresponde à densidade de energia compreendida entre 51-54 e 58-63 J/mm$^3$. As peças revelaram uma microestrutura não homogénea com contornos de grão bem definidos. Relativamente ao buraco interno da peça, as peças cuja densidade de energia está compreendida entre 45-53 e 70-73 J/mm$^3$ exibiram a melhor precisão dimensional, ou seja, menor acúmulo de pó. Futuramente seria interessante continuar a otimizar os parâmetros de impressão, afunilando-os de impressão para impressão, até serem atingidos os valores ótimos para estes novos materiais emergentes no ramo biomédico.



**Palavras-Chave:** Ferro puro, Fabrico aditivo, Parâmetros L-PBF, Otimização, Implantes ósseos

## Abstract

Additive Manufacturing (AM) technology, also known as 3D Printing, has revolutionized medical engineering, particularly in the manufacture of scaffolds - three-dimensional structures that offer temporary support for the growth and regeneration of new bone tissue. These structures are highly customizable and have high anatomical adherence, enabling more effective integration with the body. In general, scaffolds have a cellular structure, formed by pores and channels that facilitate the penetration of cells and tissues into their structure. However, due to the geometric complexity of these components, establishing optimal manufacturing parameters becomes an arduous and time-consuming task. In addition, the mechanical properties of these materials as a function of printing and design parameters are not yet fully understood. This master's thesis sought to contribute to filling the knowledge gaps in these areas of study. This work follows on from a previous project on a larger scale, in which experiments were carried out in terms of the design of the parts and the study of their mechanical properties as a function of the chosen parameters. Therefore, this dissertation is a continuation of that project, in which the information obtained from the 3D prints made previously serves as a starting point. Experimentally, a new 3D print was started, using the laser powder bed fusion method, with a different geometry, of which 144 parts are part, all of them originated by different printing parameters. This work is divided into two main tasks: (i) analysis of the powder used in the printing; (ii) analysis of the printed parts. In the first stage, the size and morphology of the powder particles were analysed using the DLS and SEM methods, respectively. In the second stage of the work, the printed parts were the target of study, in which: (i) porosity measurement; (ii) hardness measurement; (iii) microstructure analysis; (iv) analysis of the dimensional accuracy of the inner hole; and roughness measurement/analysis were carried out. It should be noted that these analyses were always aimed at associating the direct influence that the printing parameters have on the mechanical properties and characteristics of the geometry of the parts. The results showed exactly that, that there is a direct relationship between both factors. The powder analysis revealed a material with very irregular particles and a size almost three times larger than that advertised by the manufacturer. The porosity tests revealed that the best results correspond to parts with energy densities between 51-54 and 58-63 J/mm$^3$. For hardness, the optimum range is between 45-59 J/mm$^3$. For both, the printing speed parameter was the most decisive, with the best results coming from 600-800 mm/s. Since porosity and hardness are the most important characteristics to take into account in order to achieve the desired bone implants, requiring parts that are as dense as possible and of considerable hardness, it can be concluded from this that the optimum window of results corresponds to an energy density of between 51-54 and 58-63 J/mm$^3$. The parts showed an inhomogeneous microstructure with well-defined grain contours. With regard to the internal hole in the part, the parts with an energy density between 45-53 and 70-73 J/mm$^3$ showed the best dimensional accuracy, i.e. the least accumulation of dust. In the future, it would be interesting to continue optimizing the printing parameters, tapering them from print to print, until the optimum values are reached for these new materials emerging in the biomedical field.



**Keywords:** Pure iron, Additive Manufacturing, L-PBF parameters, Optimization, Bone Implants

# Agradecimentos/Acknowledgements

This work was supported by FCT (Fundação para a Ciência e Tecnologia), within the project PTDC/CTM-CTM/3354/2021 “Biodegradable implants in porous iron obtained by additive manufacturing”.

Uma dissertação de mestrado é o resultado de um esforço coletivo, pelo que, gostaria de expressar a minha gratidão a todas as pessoas que de alguma forma contribuíram para a sua realização.

Em primeiro lugar, agradeço ao projeto em si e ao meu orientador, Professor Jorge Lino, pela oportunidade que me proporcionou de integrar este projeto, por todo o acompanhamento e disponibilidade demonstrada ao longo de todo o processo. Gostaria também de deixar um agradecimento especial ao Pedro Lopes, pela sua orientação, pela disponibilidade que sempre demonstrou para comigo e pelos conselhos práticos.

À Emília Soares, do Departamento de Engenharia Mecânica, expresso a minha gratidão pela sua ajuda na preparação das amostras e pela sua sempre pronta disponibilidade. Ao Engenheiro Rui Silva, do laboratório de Ensaios Tecnológicos, agradeço a disponibilidade prestada na realização dos ensaios de dureza.

Aos meus pais, aos meus Avós e à minha irmã, quero agradecer o apoio incondicional e as palavras de incentivo. Obrigada por estarem sempre aqui para mim.

Por fim, mas não menos importante, à Inês e aos meus amigos, agradeço por serem uma parte essencial da minha vida e por me apoiarem em todos os momentos.

## United Nations Sustainable Development Goals (SDGs)

| SDG | Target | Contribution | Performance Indicators and Metrics |
|---|---|---|---|
| 3 | 3.4 | Development of biocompatible and strong scaffolds for bone regeneration | Improved patient outcomes; scaffold biocompatibility and strength |
| 9 | 9.5 | Optimization of L-PBF parameters for improved medical applications | Number of successful prints; enhanced mechanical properties |
| 12 | 12.5 | Reduction of material waste through optimized printing | Lower defect rate; better resource efficiency |

# Contents

# Acronyms and Symbols

| | |
|---|---|
| 3D | Three-Dimensional |
| AM | Additive Manufacturing |
| BTE | Bone Tissue Engineering |
| CAD/CAM | Computer-Aided Design/Manufacturing |
| DEMec | Departamento de Engenharia Mecânica |
| DLS | Digital Light Scattering |
| DNA | Deoxyribonucleic Acid |
| EDS | Energy Dispersive Spectroscopy |
| INEGI | Institute of Science and Innovation in Mechanical and Industrial Engineering |
| ISO/ASTM | International Organization for Standardization & The American Society for Testing and Materials |
| L-PBF | Laser Powder Bed Fusion |
| Ra | Average Roughness |
| SEM | Scanning Electron Microscope |
| SLM | Selective Laser Melting |
| STL | Stereolithography |
| VED | Volumetric Energy Density |

# List of Figures

# List of Tables

# 1. Project GradImp and Contextualization of Dissertation

This work was funded by FCT (Fundação para a Ciência e Tecnologia) as part of the project PTDC/CTM-CTM/3354/2021, titled “Biodegradable implants in porous iron obtained by additive manufacturing.” This project is a collaboration between the *Faculdade de Medicina da Universidade do Porto, Instituto Superior Técnico, Instituto de Ciência e Inovação em Engenharia Mecânica e Engenharia Industrial,* and *Instituto Politécnico de Setúbal.*

The primary goal of this project is to develop a new concept for biodegradable temporary iron implants that integrate an enhanced degradation rate, improved mechanical performance, and increased biocompatibility. This is achieved through an innovative graded design with different cellular structures, in contrast to compact iron, along with an advanced manufacturing technique, Laser Powder Bed Fusion (L-PBF), which allows the fabrication of intricate structures with high precision.

However, to successfully manufacture optimized bone scaffolds using L-PBF technology, it is essential to understand the various stages of the production process and how different process parameters and geometries affect the mechanical properties of the material. This requires a comprehensive study of each variable and the exploration of multiple cellular structure possibilities.

Thus, this dissertation is based on previous research carried out as part of this project, in which 3D prints were previously developed with simpler geometries and broader printing parameters. The data and conclusions from that previous work served as the basis for this dissertation, in which a new 3D print of a more complex structure with refined printing parameters was started. The aim is to analyse the resulting parts and understand how the various printing processes and part geometry influence the mechanical properties of the material, in order to further optimize the parameters.

# 2. Literature Review

## 2.1 Bone Implants

One component of living things with an innate ability to regenerate is bone. Bone fractures and cracks that are smaller than a key threshold size can heal on their own; greater than that, they cannot. As a result, serious wounds or infections could occur, necessitating medical interventions to help the bone heal and return to its original form and function [1]. In situations like these, bone-graft materials are frequently needed to generate an osteogenic response that encourages the growth of new bone [2].

Numerous materials for bone implants, including biopolymers, bioceramics, and biomedical metals, have been created to date (Figure 1) [3,4]. One class of material with strong biocompatibility and plasticity is biopolymers. Nevertheless, their applicability in bone regeneration is limited by their low strength, poor hydrophilicity, and risk of aseptic inflammation [5]. Bioceramics with high compatibility and activity are typically constrained by their brittleness. Biomedical metals have integrated mechanical qualities that make them more appropriate for load-bearing applications when compared to biopolymers and bioceramics. Cobalt-chromium alloys, stainless steels, and titanium alloys are often utilized metals in medical applications. Although these metals can act as partially functional replacements for natural bones, they cannot be degraded and they become permanent implants [6]. Consequently, as the bone heals, a second procedure is always required to remove these implants. Patients will almost certainly experience more pain and expenses after multiple surgeries [7]. Therefore, scientists are looking into biomedical metals that can gradually break down in the human body and then dissolve entirely without leaving any trace after bone regeneration, thus avoiding the need for a second surgery [8].

The topic of biodegradable metals will be discussed in more detail in subsection 2.2.

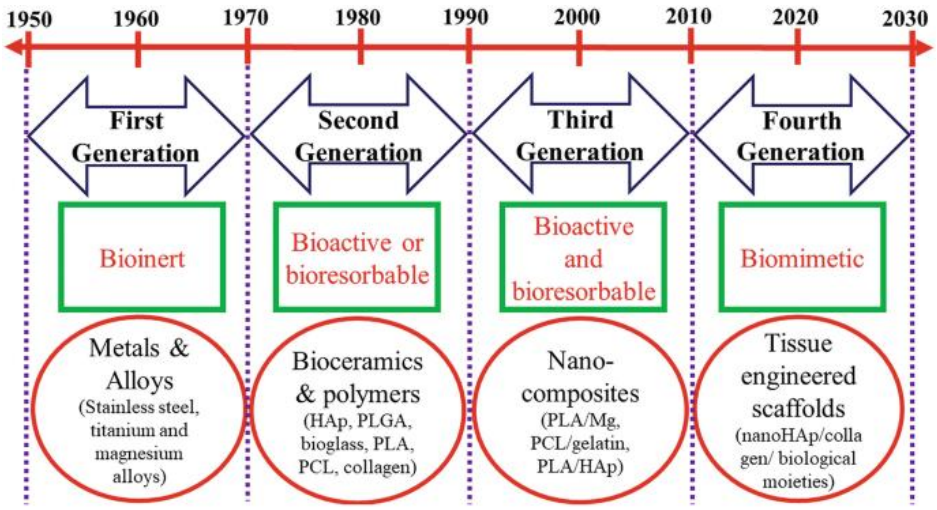


Figure 1 - Evolution of biomaterials for bone implants [9]

### 2.1.1 Bone Tissue

The skeleton stores calcium and serves as a structure, a barrier, and a means of locomotion. A combination of inorganic and organic phases compose bone [10]. Bone's structure and composition is presented in Figure 2.

Type I collagen fibres, glycoproteins, proteoglycans, g-carboxylated (gla) proteins, and water make up the bone matrix. Numerous non-collagenous proteins play physiological roles in the control of mineralization or bone cell activity. One α(II) chain and two identical α(I) chains make up the triple-helical molecule that is type I collagen (polymer). Mature bone's collagen fibres are arranged in alternating layers, giving the structure its maximal strength (lamellar bone) [11]. Collagen type I (COL-I) makes up around 30% of the organic components, whereas calcium phosphates in the form of hydroxyapatite ($Ca_{10}(PO_4)_6(OH)_2$, HA) (ceramic) make up the majority of the inorganic components. The mechanical strength and durability that define bone are produced by the organic and inorganic phases' nanoscale structure. Osteoblasts manufacture collagen microfibrils, which aggregate laterally and longitudinally to form fibers known as osteoids. Biomineralization is the term for the process by which the osteoblasts place HA crystals into the spaces between the collagen fibrils. The mechanical characteristics of bone tissue are determined by the degree of

biomineralization; a larger degree of mineralized bone matrix results in a stronger structure, but one that is more susceptible to fracture.

Trabecular and cortical bone are the two primary types of bone. The bone types differ from each other by their structure. About 80% of the bone in the adult skeleton is cortical, and the other 20% is trabecular. The primary functions of cortical bone, which is highly calcified, are structural and protective. Because trabecular bone has a larger surface area and is less highly calcified, it can be more metabolically active [11]. Each skeletal site has a different ratio of trabecular to cortical bone. For instance, vertebrae contain a lot of trabecular bone but very little cortex, whereas long bones have a lot thicker cortices and comparatively less trabecular bone. While trabecular or cancellous bone has a bigger porosity between 30% and 90% and a lower compressive strength of 2–12 MPa, cortical, also known as compact bone, has a porosity between 5% and 30% and a compressive strength of 70–280 MPa [12,13].

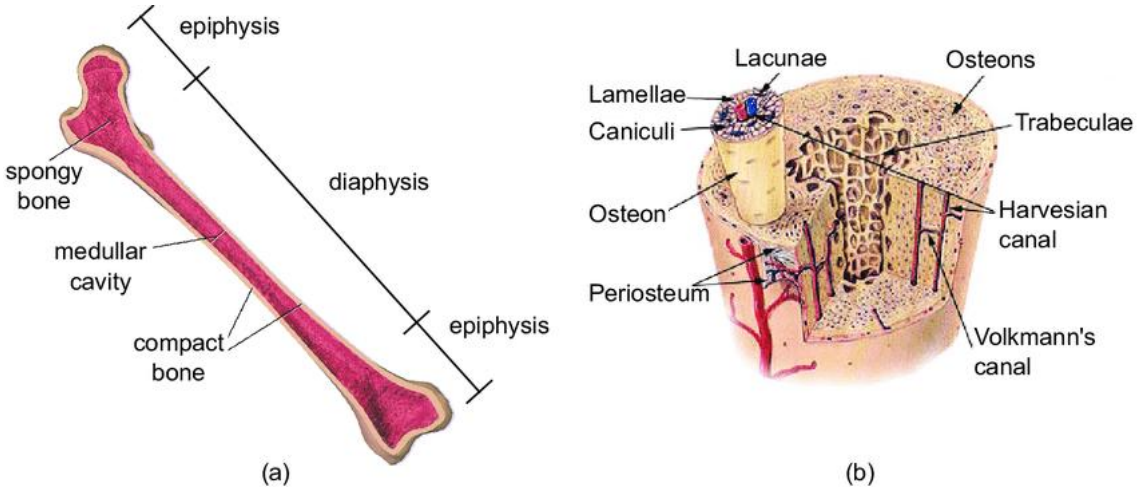


Figure 2 - (a) Long bone structure; (b) Bone composition [14]

### 2.1.2 Mechanical properties of bone

Despite being an organic substance, bone is frequently compared to artificial engineering materials. Nevertheless, it is likely to exhibit greater fluctuation in measured properties than usual engineering materials due to the nature of its synthesis. Among the factors are age; gender; location in the body; temperature; mineral content; amount of water present; disease; etc.

There may be some degree of interdependence between these variables. For instance, the mineral composition will change depending on the patient's age and the location of the bone in the body. The density and strength of human bones normally decline with age, making them more prone to fracture. Osteoporosis is a condition characterized by a significant loss of bone mass that primarily affects women who have gone through menopause. Due to these variables, the parameters measured of bone can vary, hence the numbers in tables are always an average [15].

Furthermore, because of its anisotropic structure, bone's mechanical properties need to be taken into account in two orthogonal directions:

- Longitudinal: in line with the alignment of the osteon. This is the typical loading direction.
- Transverse: at right angles to the bone's long axis.

- **Density**

In average, bones have values of density between 1.7 and 2.0 g/cm$^3$ [16].

- **Young's Modulus**

Table 1 displays the actual values for the Young's modulus of bone in comparison with hydroxyapatite and collagen. Young's modulus is also dependent on temperature; its measured value decreases as temperature rises and its value increases as strain rate increases [15].

Table 1 - Young's modulus of bone [15]

| Material | Young's Modulus, E (GPa) |
|---|---|
| Collagen (dry) | 6 |
| Bone mineral (Hydroxyapatite) | 80 |
| Cortical bone, longitudinal | 11 - 21 |
| Cortical bone, transverse | 5 - 13 |

The Young´s modulus of trabecular bone is between 0.05 and 0.5 GPa [17].

- **Tensile and Compressive Strength**

Normal loading can cause bending moments in bones, like the femur. In various areas of the bone, these induce compressive and tensile stresses [15]. Table 2 shows stress values for bones.

Table 2 - Stress values for cortical bone [15]

| | Longitudinal direction | Transverse direction |
|---|---|---|
| **Tensile strength (MPa)** | 60 - 70 | ~ 50 |
| **Compressive strength (MPa)** | 70 - 280 | ~ 50 |

The tensile strength of trabecular bone is between 10 and 20 MPa and its compressive strength is between 2 and 12 MPa [17].

- **Elasticity**

When tested under moist conditions in either compression or tension, compact bone typically exhibits stress-strain curves that roughly resemble a straight line.

As bone often only achieves a maximum total elongation of 0.5-3%, it is classified as a brittle solid rather than a ductile one [15].

- **Fracture Toughness**

Transverse toughness values are often higher than longitudinal toughness values, which is in contrast to the results for tensile and compressive strength and modulus. The cement lines that are present in the microstructure are the cause of this. These are the weakest parts of bone; they are the thin areas surrounding the outermost lamellae in the osteons. Crack propagation parallel to the osteons can occur much more easily through these areas and this significantly affects the fracture toughness of cortical bone in the longitudinal direction. When a fracture approaches a cement line, it will reorient itself and become blunted if it is spreading perpendicular to an osteon [15].

Because of this, bone has exceptional toughness while being categorized as a brittle material (with mineral as the main component). When measured parallel to the grain, the fracture toughness of bone is between 2 and 12 $MPa.m^{1/2}$, which is similar to that of wood and steel at low temperatures [17].

This review of the literature on bone is crucial to the development of this project because when designing biocompatible materials like pure iron, a promising biodegradable implant because of its advantageous degradation and bone regeneration properties, it requires an understanding of bone biology and mechanics. The mechanical properties of bone, such as its strength and elastic modulus and its density, are important standards for creating metallic biomaterials. By controlling microstructure and porosity through L-PBF parameter optimization, pure iron implants can minimize stress shielding, improve biological integration, and achieve the necessary mechanical properties.

### 2.1.3 Bone tissue engineering

Large bone defects that are beyond the natural regenerative capacity of human bones are the focus of bone tissue engineering (BTE). In order to support tissue regeneration and repair, this field integrates cells, signalling molecules, and biomaterial scaffolds [18]. The scaffold serves as an essential framework that promotes tissue growth, differentiation, and cell proliferation. It is intended to degrade over time, allowing the regenerated bone to take its place.

High porosity and gradient pore structures for nutrient and cell transport, mechanical qualities appropriate for bone support, biocompatibility to avoid negative reactions, and biodegradability to permit integration with new tissue are all essential components of an efficient scaffold. These scaffolds are precisely customized to fit a range of shapes and sizes thanks to the use of cutting-edge technologies in their design and construction, such as computer-aided design and manufacturing (CAD/CAM) [18,19].

Biomaterials are essential for scaffolds because they have properties like high compatibility with living tissues, ease of processing, and non-toxicity. Biodegradable and biocompatible materials have been prioritized in recent developments, guaranteeing scaffolds facilitate effective bone regeneration and repair. The significance of material selection in improving scaffold performance and clinical outcomes is highlighted by this focus [18].

### 2.1.4 Pore Size and Porosity

Pore size and porosity have a major impact on osteoconductivity, which is closely related to the osseointegration potential of implants. Optimizing these factors is essential to the design of porous scaffolds during fabrication. According to early research, basic cellular functions require a pore size of at least 100 μm. Nonetheless, recent research has shown that scaffolds with pore sizes larger than 300 μm improve vascularization, and that a pore size of at least 300 μm is recommended as well for efficient osteointegration. This threshold promotes capillary formation, nutrient transport, and cell migration—all of which advance osteogenesis [20].

In addition to pore size, porosity is crucial for scaffold performance. Scaffolds with porosity levels between 70% and 90%, which are similar to those of human trabecular bone, support bone ingrowth and cell viability. High porosity (>60%) has been widely regarded as beneficial for osteogenesis by increasing the surface area, which aids in osseointegration, nutrient delivery, and cell migration [21]. Nonetheless, porosity also has an impact on scaffolds' mechanical properties. Increased porosity diminishes

mechanical strength while bringing metal scaffolds' elastic modulus into line with bone's, which reduces the effects of stress shielding [22].

Laser-based powder bed fusion (L-PBF) has emerged as a promising technique for scaffold production due to its stability, efficiency, and precise control over internal pore architecture. This technology makes it possible to carefully adjust important structural parameters that are necessary to achieve the best mechanical and biological properties in implants, such as strut diameter, pore geometry, size and interconnectivity [22].

In general, the design of biomaterial scaffolds relies heavily on the interaction between pore size and porosity. These elements have a significant impact on cell behavior, vascularization, and bone formation both in vitro and in vivo, in addition to influencing the mechanical behavior of the implant.

### 2.1.5 Lattice structures

Lattice structures, also known as lattice or cellular materials, consist of space-filling unit cells tessellated along axes without gaps [23]. Their remarkable properties, such as high specific stiffness and strength, lightweight design, energy absorption, and acoustic insulation, make them widely used. Applications include load-bearing components, implants, heat exchangers, and filters [24]. The architecture of these structures affects their mechanical behavior and performance, and they are classified according to the type of porosity (open or closed) and the order of unit cells (stochastic or non-stochastic), which means random or periodic, respectively (Figure 3). Typical examples of cellular materials include foam, sponges, honeycomb, and folded materials [25]. The most significant lattice structures are shown in Figure 4.

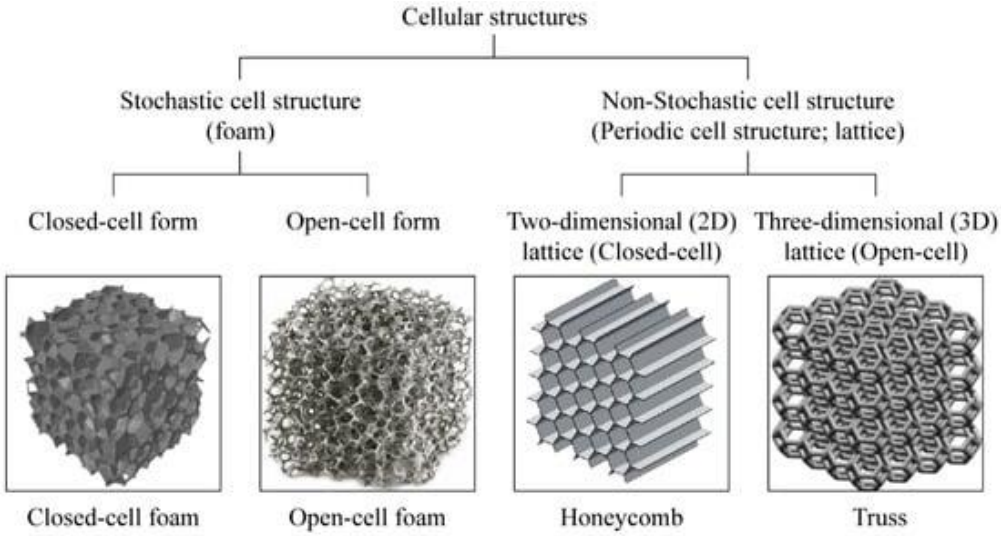


Figure 3 - Categories of cellular structures [26]

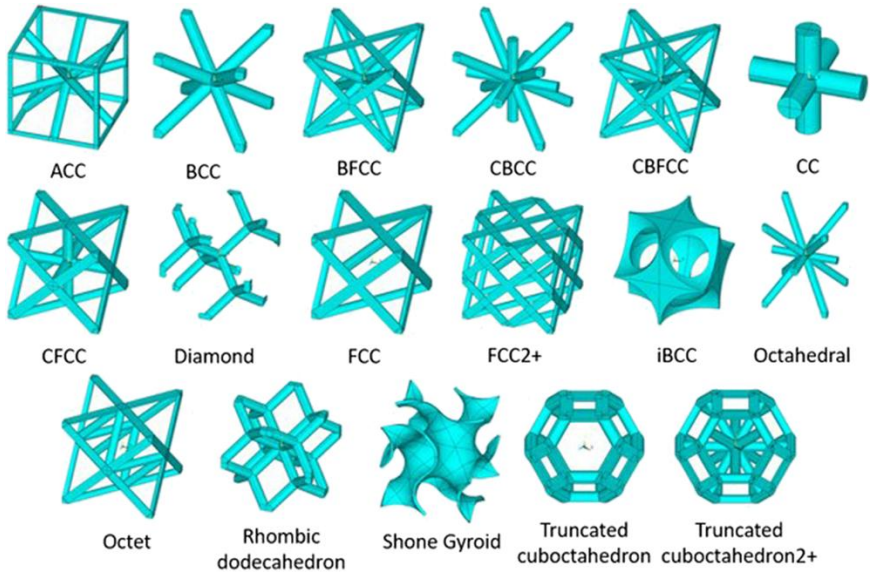


Figure 4 - Examples of lattice structure unit cells [27]

The production of lattice structures has advanced significantly thanks to additive manufacturing (AM) technologies, particularly L-PBF. AM outperforms traditional techniques like casting or forming, which have fewer design options and frequently call for complex assembly procedures, by providing precise control over unit cell geometry, strut thickness, and material usage [24]. AM is especially useful in biomedical applications because it allows for high porosity, which supports bone ingrowth, osseointegration, regeneration, and structural stability on lattice structures [28]. However,

L-PBF lattice structure failure is largely caused by geometric defects like strut waviness, strut thickness fluctuation, and strut oversizing. Achieving ideal lattice structures with desired properties requires careful consideration of process parameters, unit cell structures, and materials [29].

## 2.2 Biomaterials for Advanced Manufacturing

The development of biomaterials has progressed through three generations. Bioinert materials for structural support and attachment were the main emphasis of the first generation. Bioactive and biodegradable qualities were introduced by second-generation biomaterials. The third generation focuses on using bioinstructive materials to create a biological environment that promotes bone regeneration [30]. Utilized in BTE, these scaffolds combine growth factors and cells to promote healing while preserving mechanical strength, biodegradability, bioactivity and bioinertness [31]. Even with these developments, choosing the best biomaterial to treat every kind of bone lesion is still very difficult.

In general biomaterials are categorized as ceramics, polymers, metals and composites. Each material has certain qualities and benefits that make it appropriate for specific purposes in the biomedical sector.

### 2.2.1 Ceramics

Due to its remarkable qualities, such as their high strength, chemical inertness, biocompatibility, and resistance to wear, ceramic materials are highly prized in dental and biomedical applications. Because of their resilience in harsh conditions, they are frequently utilized for crowns, bridges, and implants. The production of microscale parts with outstanding mechanical qualities was a challenge for traditional ceramic processing, but AM has changed this by making it possible to fabricate ceramic components that are micron-sized and have improved strength and accuracy [32].

Bioceramics are potential materials for BTE because of their favourable properties, which include biocompatibility, biodegradability, osteoconduction, osteoinduction, and hierarchical porosity. Their commercial success has been limited, nonetheless, by disadvantages such as high brittleness, quick deterioration compared to bone growth, and mechanical instability. Their application is currently restricted to bone fillers like cements and tiny, non-load-bearing implants. To overcome these obstacles and enable bioceramics to sustain load-bearing applications and attain wider commercial viability, more research is required [33,34].

The most common ceramics used in biomedical field are hydroxyapatite, zirconia, alumina, and bioactive glasses.

### 2.2.2 Polymers

Since polymers have desirable properties including controlled biodegradation, high porosity, mechanical strength, and design flexibility that allows them to be molded into diverse shapes, they are widely utilized biomaterials in scaffold fabrication for both soft and hard tissue regeneration. The two main categories of polymers are synthetic and natural. Because of their innate bioactive qualities and biocompatibility, natural polymers derived from proteins (such as silk fibroin and gelatin) and polysaccharides (like chitosan and alginate) closely resemble the extracellular matrix (ECM). Among natural polymers, silk fibroin is unique due to its remarkable mechanical properties, slow disintegration rate, and thermal stability. However, there are drawbacks to natural polymers, including worse mechanical properties, restricted availability, and expensive extraction costs [35].

The advantages of synthetic polymers, such as polylactic acid (PLA), polyglycolic acid (PGA), poly(lactic-co-glycolic acid) (PLGA), and polycaprolactone (PCL), include scalability, reduced prices, and customizeable mechanical and structural characteristics. Despite having a long shelf life and strong mechanical stability, synthetic polymers can negatively affect cell growth and biocompatibility because they produce acidic byproducts during decomposition that can cause inflammation and decreased cell adhesion [36,37].

Due to their low melting points, great plasticity, and affordability, polymers have emerged as a key component in AM, allowing for the creation of complex microstructures

and shapes. Polymers' biocompatibility and biodegradability, which enable them to break down gradually as tissue heals itself, make them very valuable in biomedical applications. Because of these qualities, polymers are now essential components in tissue engineering and bioprinting, allowing for the development of tissues and organs with specific mechanical and functional features. However, issues with AM-produced biomedical polymers' performance, longevity, and recyclability still need to be tackled before they can be used more widely in healthcare [38].

### 2.2.3 Metals

With a long history of success in biomedical applications, metallic biomaterials such as cobalt-chromium (Co-Cr) alloys, titanium (Ti) and its alloys, and stainless steel 316L have been widely employed as implants for stents, valves, joint replacements, pacemakers, and more. Due to their remarkable mechanical stability, biocompatibility and fatigue strength, these conventional metals are the most widely used in orthopedic treatments. This makes them perfect for load-bearing applications and critical bone defects. However, their wider efficacy is constrained by issues like wear, corrosion susceptibility, challenging manufacturing, and occasional long-term toxicity, and also compared to biodegradable metals, they do not promote active bone regeneration [39,40].

Biodegradable metals are defined as “Metals expected to corrode gradually in vivo, with an appropriate host response elicited by released corrosion products, which can pass through or be metabolized or assimilated by cells and/or tissue, and then dissolve completely upon fulfilling the mission to assist with tissue healing with no implant residues” [41]. Emerging biodegradable metals, including magnesium (Mg), zinc (Zn), iron (Fe), and their alloys, are gaining attention for BTE. These metals are found in human bone naturally as cations, which improves their biocompatibility, bioactivity, and capacity to aid in the healing process. In addition, they offer more mechanical strength than biopolymers and bioceramics, providing structural support as they degrade over time, eliminating the need for a second surgery to remove them. By addressing some of the limitations of conventional metallic implants, this family of materials presents itself as a promising substitute for bone regeneration [42,43].

The different biodegradable metals will be discussed in more detail below.

#### 2.2.3.1 Iron

Iron is a vital trace element critical to human biology, playing roles in oxygen transport, cell growth, and RNA/DNA reduction. Despite being needed in little daily dosages (8–27 mg), its levels are strictly controlled to avoid toxicity [44,45]. In biomedical applications, iron offers high mechanical properties, comparable to 316L stainless steel, making it a strong candidate for implants. However, its slow in vivo degradation rate limits its use in biodegradable applications, as it can cause reactions similar to those of permanent implants.

To overcome these obstacles, studies were carried out and it was concluded that porous iron-based scaffolds showed faster corrosion rates and a Young's modulus closer to that of cortical bone, when compared to non-porous iron, highlighting their potential for use in bone tissue engineering. By making cellular structures it is possible to adapt the mechanical properties as well as increase the degradation rate. The researchers found that pure iron was not cytotoxic and had excellent hemocompatibility and biocompatibility [46].

#### 2.2.3.2 Zinc

Zinc is an essential trace mineral that is necessary for many body activities, such as immune response, cell division, and neurological processes. Along with being crucial for DNA functions like replication, stability, repair, and protection, it also controls proteins and enzymes. Zinc degrades at a rate slower than magnesium but faster than iron, making it a good intermediate option [6,47].

Nevertheless, this material has certain drawbacks, including lower mechanical qualities (e.g., elastic limit ~100 MPa) than iron and magnesium, which restricts its use in load-bearing situations, and zinc oxide can accumulate at the degradation site, potentially affecting local tissue reactions. Producing zinc implants using L-PBF is challenging because of zinc's low melting and boiling points, as well as its high susceptibility to oxidation, which leads to significant porosity in the manufactured components [48].

#### 2.2.3.3 Magnesium

Magnesium is the fourth most prevalent metal in the body (after calcium, potassium, and sodium) and an essential mineral that is primarily present in human bones. It is a crucial cofactor for numerous enzymes and plays a significant part in genome stabilization. Magnesium hydroxide and hydrogen gas are the non-toxic by-products of the natural degradation of magnesium induced by corrosion in the body. The risk of stress shielding is decreased because its elastic modulus (~45 GPa) is comparable to that of normal bone (~10–40 GPa) [49,50].

However, there are some disadvantages, for example, in the physiological environment, magnesium can corrode too quickly, which can result in a loss of mechanical integrity before tissue healing is complete. Gas pockets caused by excessive corrosion can prevent tissue repair [48].

Table 3 compares the different biodegradable metals.

Table 3 - Comparison between biodegradable metals [45,46]

| | **Iron (Fe)** | **Zinc (Zn)** | **Magnesium (Mg)** |
|---|---|---|---|
| **Degradation Rate** | Slow | Moderate | Fast |
| **Mechanical Strength** | High | Low | Moderate |
| **Elastic Modulus (GPa)** | ~200 (much higher than bone) | ~90 | ~45 |
| **Biological Role** | Iron metabolism | Enzyme cofactor, immune support | Bone metabolism enhancer |
| **Applications** | Stents, load-bearing implants | Stents, scaffolds | Orthopedics, stents |

### 2.2.4 Metal powders for AM

A key component of AM is the production of metal powders, which has a big impact on the effectiveness of the procedure as well as the quality of the final product. The need for successful recycling and reuse of unused powder is highlighted by the fact that AM processes usually use considerably less material than the total volume of powder used. The recycling procedure, however, can be challenging. As powders are exposed to the inherent thermal effects of AM processes, repeated use may change their physical characteristics, including flowability and grain size distribution. The physical and chemical characteristics of the powders may be directly impacted by these thermal effects. Also, while handling the powders during recycling, impurities can be introduced, such as moisture, oxide inclusions or other contaminants. Metal powders can have small agglutinations of smaller particles on their surface, called satellites, which are responsible for reducing the powder´s fluidity. The recycling process causes these satellites to gradually fuse with the larger particles [51]

A variety of defects, such as inclusions, porosities, and voids, can be introduced during the production of metallic powders. The porosities in these powders may be released into the melting pool and then trapped in the liquid metal when they are used in the L-PBF process. As a result, this may cause porosities after the solidification process. These porosities can have a major effect on the final L-PBF component's quality, influencing the part's overall performance as well as its structural integrity. Figure 5 shows the impact of powder porosity in the melt pool.

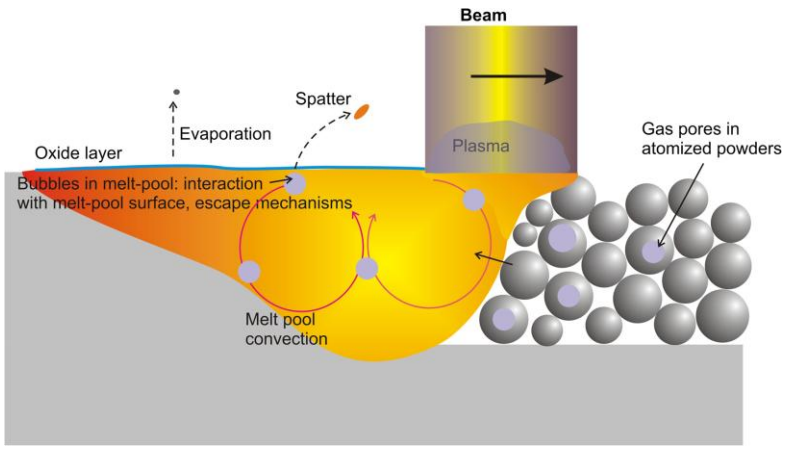


Figure 5 - Visual representation of melt pool defect phenomena in L-PBF processes [52]

Three primary steps are involved in the manufacturing of metal powders for AM. In order to create pure metals or alloys in shapes like ingots or rods, the first step involves extracting raw materials from ores or mineral resources. Using specialized production techniques, these materials are turned into powder in the second stage. Since it can create powders with desired geometric properties, atomization is the most popular of these techniques. However, post-production procedures like sieving are required to guarantee the powder satisfies the required granulometric specifications because particle size cannot be entirely controlled during production. Classifying and verifying the powders to make sure they meet the strict quality standards is the last step [53].

#### 2.2.4.1 Different methods of producing metal powders

Metal powders are made using a variety of methods. While electrolytic and chemical deposition techniques rely on chemical reactions or electrolytic processes to produce metallic particles, mechanical methods involve grinding or milling solid materials into powders. Finally, the most widely used techniques are physical ones, especially atomization [54]. The pure iron powder chosen for this project, ATOMET FeAM, produced by the Canadian company Rio Tinto, was obtained by the atomization process, more specifically, water atomization, which is why it will be the process addressed below.

Since atomization is considered the most popular, effective, and economical way to produce metal powders, it is crucial to investigate how it can produce high-quality powders for a range of uses. In order to facilitate atomization, the desired metal or alloy is initially cast, melted, and then poured. Gas, water, and plasma atomization are the three main methods of atomization. Melted metal enters a chamber and falls freely, creating spherical droplets under gravity in the process of gas and water atomization. The molten stream is then hit by jets of water or gas, which break it up into particles that cool and turn into powder. Figure 6 shows the influence of the atomization method on the sphericity of the iron powder. In contrast, plasma atomization melts and atomizes the metal using high-temperature ionized gas jets, or plasma [53,54]. Due to the plasma's controlled atomization and even heat distribution, this process yields powders with a higher degree of sphericity and a lower number of satellites, which benefits the results in

L-PBF parts when compared to other methods. The primary process for creating iron and steel powders is water atomization, which usually supplies the press-and-sintered industries instead of the specialized AM industry. It is crucial to remember that during additive processes, the oxide layers created during water atomization have a direct impact on the powder's flow characteristics and the melt's viscosity [53].

As mentioned before, the physical, mechanical, and structural integrity of the finished product are all directly impacted by the quality of metal powders, making them essential for successful additive manufacturing. For AM processes to be consistent, effective, and sustainable, advancements in powder production and recycling are crucial.

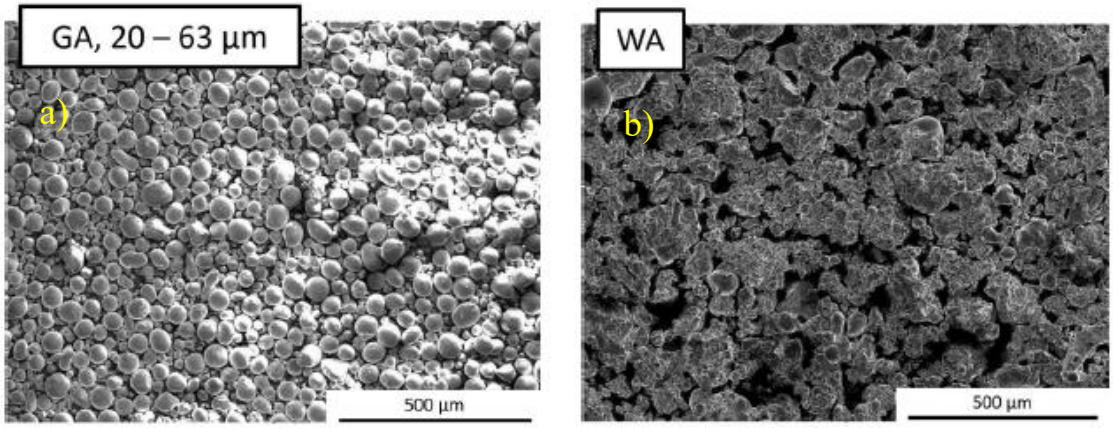


Figure 6 - Iron powder produced by: a) Gas atomization; b) Water atomization [55]

### 2.2.5 Microstructure

Each layer of material is subjected to a repeated thermal cycle in AM. A laser or electron beam is used to quickly heat the material above its melting point during L-PBF process, which is followed by quick solidification. Phase variations between layers are frequently caused by this process, which makes it difficult to precisely model and project the composition and microstructure of parts made using AM [56].

Since AM involves rapid cooling rates, it consistently produces finer-grained structures than traditional manufacturing techniques across a variety of materials. The resulting microstructure is shaped by temperature gradients, which are heavily influenced by variables like energy input, layer thickness, pre-heating conditions, and part geometry [56].

## 2.3 Additive Manufacturing

### 2.3.1 General considerations

Three-dimensional (3D) printing, also referred to as additive manufacturing (AM) technologies, initially gained attention in the 1980s. Research in this area has increased, which has accelerated the development of 3D printing technology. As a result, the market for AM has grown faster than anticipated in recent years [57].

Based on a 3D model, AM fabricates parts by directly adding materials layer by layer. Compared to conventional manufacturing methods, this technology offers several unique benefits. Rapid prototyping and the fabrication of intricately shaped pieces in a broad range of materials have made 3D printing an indispensable tool. Prototypes can be produced quickly and affordably, which speeds up the product development process. This shortens time-to-market and aids in iterative design enhancements. 3D printing methods significantly reduce material waste by producing components with nearly perfect shape and considerably higher degree of detail than traditional manufacturing processes. Additive manufacturing technology can also help to increase the dimensional accuracy. These, nonetheless, also present certain difficulties. One of the reasons is that they are unsuitable for big volume production and have a lengthy lead time for manufacturing [58].

However, these find widespread use across diverse sectors and applications, spanning from robotics to medical uses, such as prostheses production.

There are eight essential steps in the additive manufacturing process (Figure 7):

- Modelling: In which the part is designed or reverse-engineered to produce a 3D CAD file.
- STL Conversion: Converting the CAD file into the STL format for compatibility with 3D printers.
- Data Preparation / STL manipulation: Changing the orientation, size, and position of the part.
- Machine Setup: Adjusting the speed, material, and layer thickness.
- Build: Fully autonomous manufacture of the component.

- Part Removal and Cleanup: Remove the produced part when it is safe to do so.
- Post-processing: Improving the component through the elimination of supports.
- Application: Preparing the finished component, maybe with extra coatings or finishes, for its intended application.

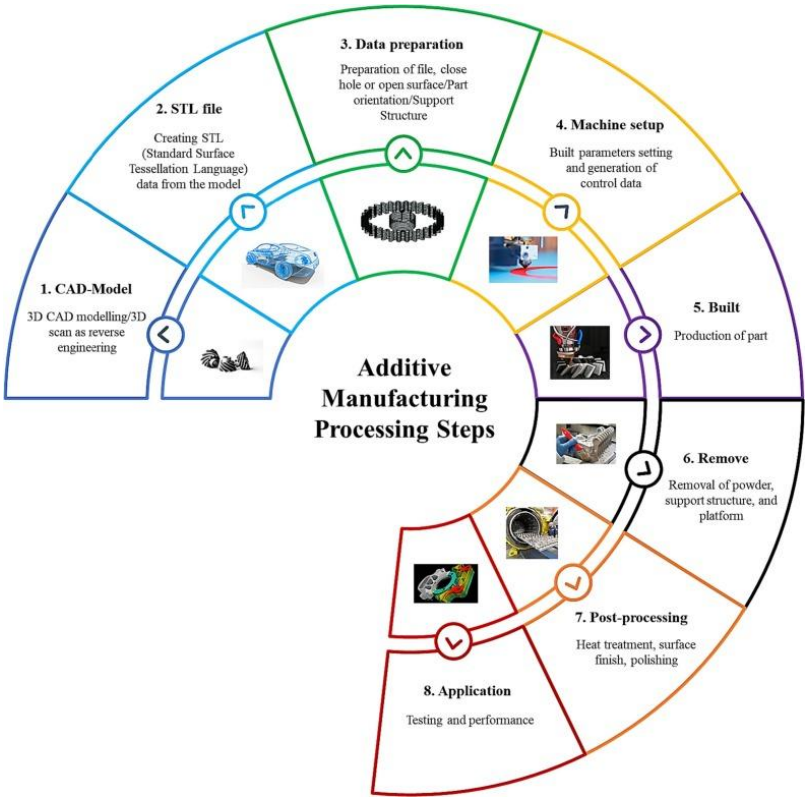


Figure 7 - Sequential steps in AM process flow [59]

In order to establish greater scientific coherence in this field, the ISO/ASTM 52900:2015 standard [60] has defined that AM can be divided into seven categories [61] (Table 4).

Table 4 - AM categories according to ISO/ASTM 52900:2015 standards

| AM Categories | Definition |
|---|---|
| Material Extrusion | A method of creating layers by pushing material via a nozzle. |
| Powder Bed Fusion | Uses a heat source, such as a laser, to fuse powder particles in a powder bed layer by layer. |
| Material Jetting | Like inkjet printing, it applies material droplets layer by layer and uses heat or UV light to solidify each layer. |
| Binder Jetting | Uses a liquid binder to selectively join powdered material layers, creating pieces that frequently need post-processing to increase their strength. |
| Directed Energy Deposition | Uses a laser or electron beam to precisely melt material (usually metal) as it is deposited; this is frequently done for large-scale manufacturing or repair. |
| Vat Photopolymerization | Uses a light source to cure liquid resin layer by layer. |
| Sheet Lamination | Uses heat or adhesives to join layers of material sheets that have been cut to shape, frequently to create composite materials. |

This project focuses on laser powder bed fusion technology which is explained in the next subchapter.

### 2.3.2 Laser Powder Bed Fusion (L-PBF)

In this AM method, a focused high-density laser beam selectively scans a powder bed. The scanned and solidified layers are then piled on top of one another to create a fully functional three-dimensional part, tool, or prototype [62].

In contrast to traditional manufacturing methods, pre-processing begins immediately with the CAD model being converted to a unique file format (.stl or other) so that triangles can be used to represent the geometry. Then, using unique algorithms, the 3D model is sliced into extremely thin layers, usually 20–100 μm in the L-PBF process. Following the configuration of process parameters based on material, required specifications, and geometry (such as scan strategy, laser power, hatch distance, and scan speed), the software of the L-PBF machine receives this slicing data and proceeds to scan each layer atop the other to build the part [63].

A powder roller applies the proper amount of powder to the building plate, as shown in Figure 8, and the laser beam is exposed to the powder selectively based on the geometry of the part. The fabrication piston drops one step at the end of each layer, while the powder delivery piston moves one step/layer up. The powder is subjected to a laser beam with enough energy to melt it. This process continues until the last layer is printed and the part is finished. After that, parts usually go through a finishing process, such as support removal, polishing, etc [64].

Inside the machine chamber, the environment is pressurized and controlled, filled with an inert gas, usually argon or nitrogen, in order to prevent oxidation of the molten metal and other undesirable chemical reactions that may occur. To further improve the process and protect machine operators, temperature control and filtering technologies are used.

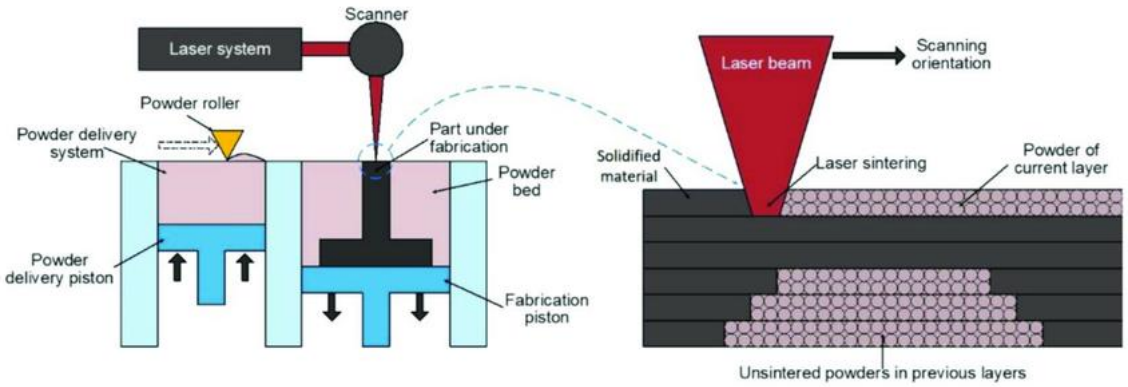


Figure 8 - Schematic diagram of laser powder bed fusion process [64]

The applications of the big family of laser-based powder bed techniques are diverse and extend to a wide range of different domains, such as aerospace, medicine and biotechnology, automotive, energy industry, military industry, electronics industry, among others [65,66].

This method, which falls under the category of "non-classic" manufacturing techniques within metal-AM, has found application in the biomedical industry. The creation of jaw and bone implants for use in dentistry and orthopaedics is among the earliest research fields [67,68].

### 2.3.3 Printing parameters for the L-PBF process

The L-PBF process involves a wide range of physical phenomena, including as heat transfers, fluid flow, vaporization, material emission, chemical reactions, and laser absorption and reflection. Both liquid-to-solid and powder-to-liquid phase transitions take place simultaneously. Understanding these physical phenomena can help in the efficient manufacture of components that are very close to the desired goal, i.e. without defects and the selection of suitable process parameters for the L-PBF procedure [69].

The L-PBF process is controlled by various parameters, as shown in Figure 9.

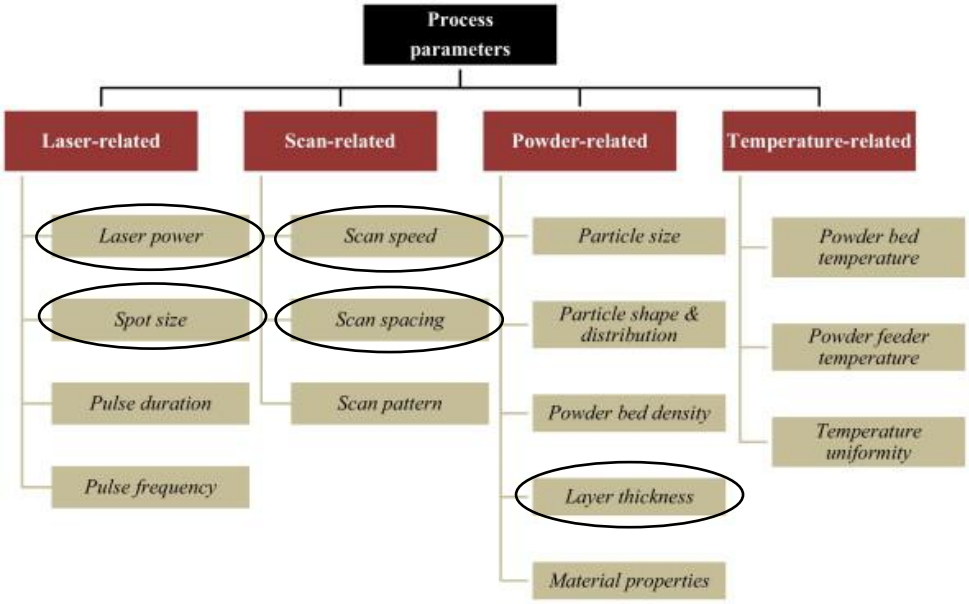


Figure 9 - L-PBF process parameters [70]

As can be seen highlighted in figure 9, scanning speed, hatch spacing, laser power, layer thickness and spot size are the main build parameters that impact laser powder bed fusion. They play a critical role in determining the quality, mechanical properties and efficiency of the final part, so the focus will be on them [71]. These parameters are shown schematically in Figure 10.

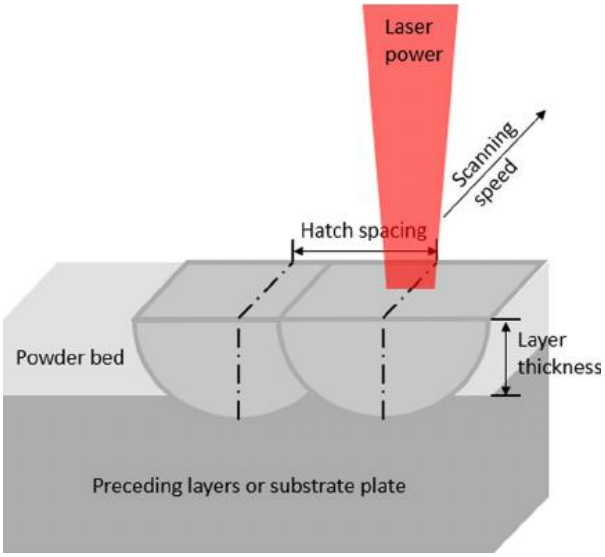


Figure 10 - Schematic representation of L-PBF process parameters [72]

- Scanning Speed: The speed at which the laser moves across the powder bed during the melting process.
- Hatch Spacing: The distance between adjacent laser scan lines in a single layer.
- Laser Power: The amount of energy output by the laser during the L-PBF process, typically measured in watts (W).
- Layer Thickness: The thickness of a layer that equals one incremental amount of the powder bed.
- Spot Size: The diameter of the laser beam at the focal point where it interacts with the powder bed.

It is difficult to determine the exact magnitude of each parameter level in the L-PBF process because every response is affected by every process parameter. Rather than precise values, the parameter ranges are typically controlled by volumetric energy density (VED) equations. VED, which stands for the energy that the laser applies to a unit volume of powder, is an important consideration in the production process of melting powder materials. This parameter establishes a relationship between the laser beam's energy and key process parameters like scanning speed, hatch spacing, laser power, and layer thickness, ensuring their combined effect is appropriately controlled.

An identical energy density value with different L-PBF process parameters results in different material properties. Essentially, the nuances of energy input and how it interacts with the material are not completely captured by the VED equation alone. Even

when the VED is the same, the resulting material properties are highly dependent on the particular process settings because each parameter has a distinct impact on the heat distribution, melt pool dynamics, and solidification behavior [29].

The empirical formula of VED is calculated using Eq. (1):

$$VED = \frac{P}{Vs \times Dh \times t} \quad (1)$$

where:

VED, is the Volumetric energy density (J/mm$^3$),

P, is the laser power (W),

Vs, is the scanning speed (mm/sec),

Dh, is the hatching distance (mm), and

t, is the layer thickness (mm).

In addition to VED, Energy Intensity (I) is another crucial parameter that considers both the amount of energy delivered and its distribution within the impact area of the laser [29]. The energy intensity is defined as the laser power distributed over the focal area of the laser beam. It can be expressed as shown in Eq. (2):

$$I = \frac{P}{A} \quad (2)$$

where:

I, is the Energy Intensity (W/mm$^2$),

P, is the laser power (W), and

A, is the cross-sectional area of the beam (mm$^2$), assumed to be a circle, calculated as:

$$A = \pi \times \left(\frac{d}{2}\right)^2 \quad (3)$$

where:

d, is the spot size (mm)

Thus, the final Energy Intensity formula is expressed as:

$$I = \frac{P}{\pi \times \left(\frac{d}{2}\right)^2} \quad (4)$$

### 2.3.4 Defects in the L-PBF process

As mentioned before, the L-PBF process relies on a variety of interrelated parameters, powder characteristics and the chamber environment. If any of these factors are not properly configured, defects are likely to occur [73]. Under-heating and overheating melting processes on overhang structures or unsteadily melting parts are the most common causes of defects in the L-PBF process [29]. Some of the significant defects influencing the result of the L-PBF parts are discussed below.

- **Balling:** A phenomenon which is usually brought on by not sufficient wetting of the melt pool, occurs when molten metal forms spherical droplets rather than a smooth layer. This can occur due to the combination of a moderate laser power and a low scanning speed (first type of balling) or due to the combination of a high laser power and a high scanning speed (second type of balling) [74, 75]. Figure 11 shows balling effects.

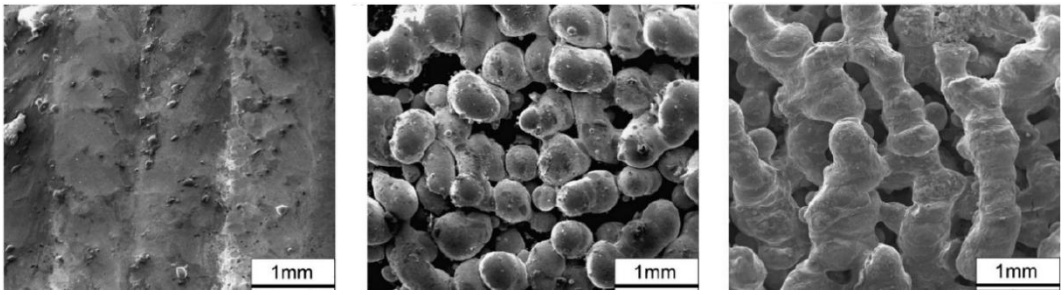


Figure 11 - Surface morphologies characteristic of: (left) no balling; (middle) second type of balling; (right) first type of balling [76]

- **Cracking**: Cracks arise from high thermal gradients and residual stresses, especially in materials with low ductility or poor thermal conductivity. They can propagate through the part and cause failure, mitigated by preheating, optimized scanning, or material selection (figure 12 (a) and (b)) [73].

- **Delamination**: Refers to layer separation, which is frequently brought on by inadequate bonding from low energy input or incorrect laser scan overlap (Figure 12 (c)). As residual stress weakens interlayer adhesion, it can make this defect worse [75].

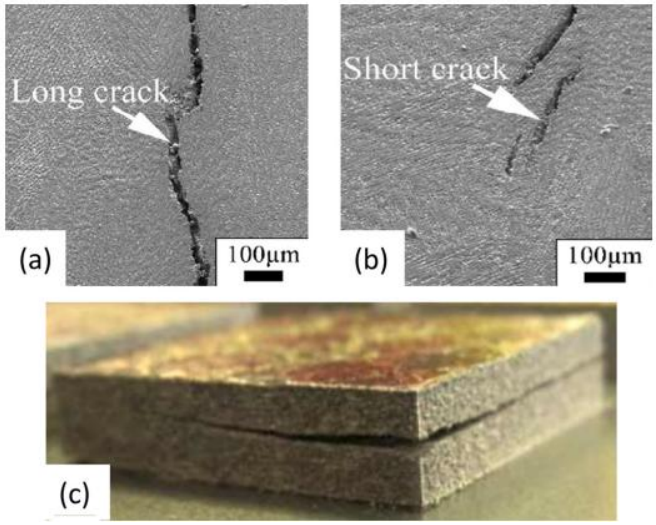


Figure 12 - SEM images of examples of cracking: (a) long crack, (b) short crack; (c) example of delamination between layers [77]

- **Swelling**: Occurs when localized over-melting caused by excessive heat input results in bulges in the material. This flaw causes uneven material distribution and is associated with improper laser parameters or poor powder flow. This phenomenon is similar to the balling phenomenon, but in this case the metal does not solidify into spherical shapes, but into ripples causing surface relief (Figure 13).

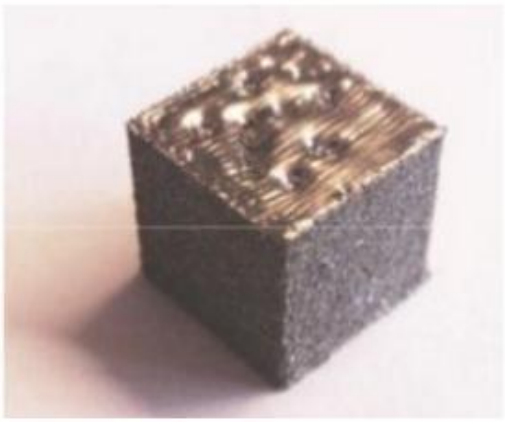

Figure 13 - Swelling phenomenon [77]

- **Warping**: Uneven thermal contraction and expansion during rapid cooling results in part deformation. For thin structures or overhanging geometries, this is particularly problematic (Figure 14) [75].

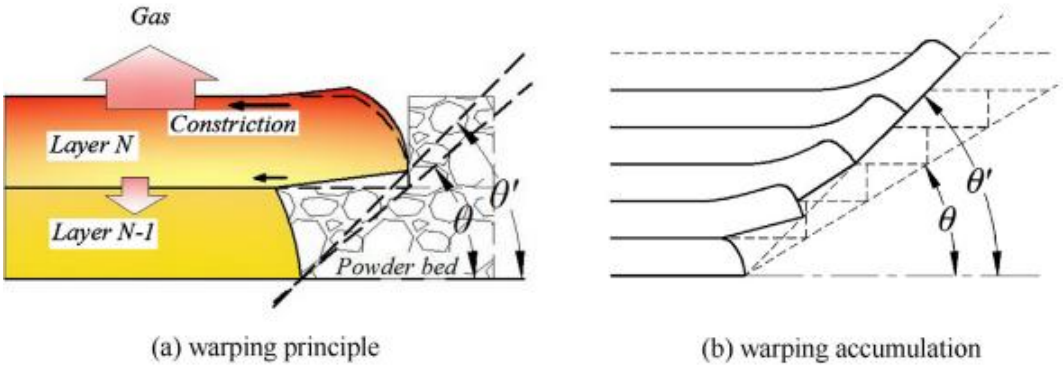


Figure 14 - The warping principle during L-PBF fabrication of overhanging surface [78]

- **Surface roughness**: Is an anomaly where partially melted particles stick to the part's surface (Figure 15); this often comes on by melt pool spatter or not sufficient powder layer recoating. Inadequate powder properties or inappropriate scanning techniques may also be the cause [74].

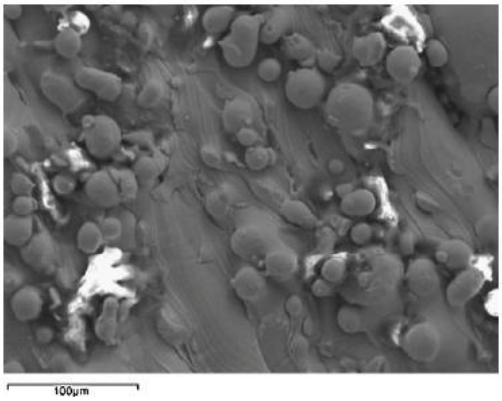


Figure 15 - Presence of particles in a part made by L-PBF [79]

- **Loss of alloying elements**: Happens when volatile elements are vaporized by high laser power or extended laser beam exposure, changing the composition of the material and compromising mechanical performance [74].

- **Distortions**: Are widespread deformations of the component caused by the buildup of residual stress, which may be brought on by irregular heat distribution and thermal cycling.

- **Residual stress:** Is a common problem in L-PBF that results from high thermal gradients and quick solidification (Figure 16 - top). During or after printing, these stresses may cause cracks, warping, or even failure, requiring post-process stress-relieving treatments (Figure 16 - bottom) [74].

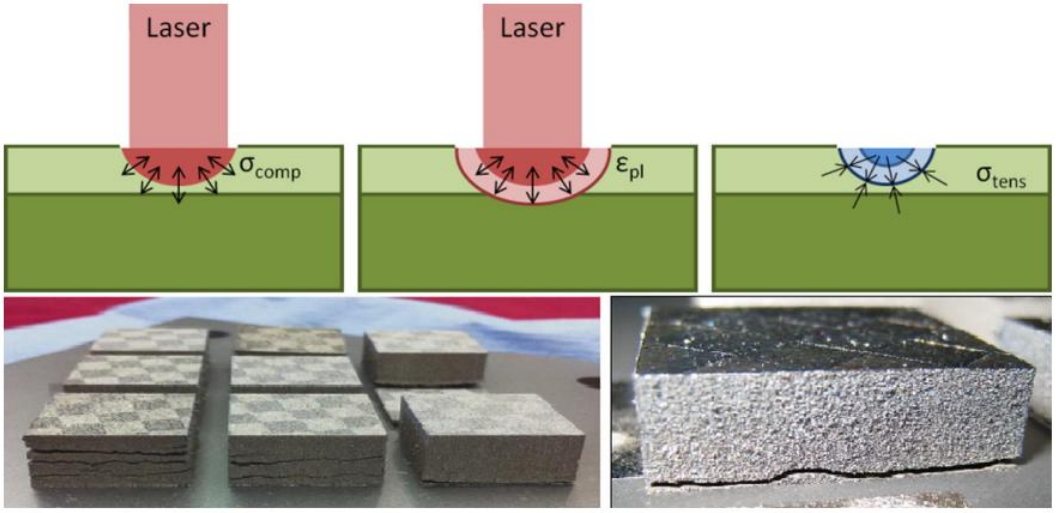


Figure 16 - Temperature gradient mechanism (top) leading to the formation of cracks and delamination (bottom) [72]

The mechanical properties of the L-PBF-fabricated parts, particularly fatigue strength, are greatly impacted by defect formation. Defects directly shorten a part's fatigue life and are a major factor in the beginning of fatigue cracks, which limits the use of this process. Defect identification and elimination are the basis of quality control in an L-PBF process. High-quality fabrications require real-time flaw reduction, simulation, modeling, and defect monitoring. In the near future, defect-free L-PBF productions are expected [73].

In summary, this literature review was essential for the preparation of this work, since the optimization of L-PBF parameters for pure iron implants requires knowledge of pore size, porosity and biomaterials, since these factors have an impact on biocompatibility, degradation and mechanical properties. In addition, the evaluation of material properties that affect part quality and process stability is facilitated by research into metal powder production techniques.

Optimizing manufacturing conditions and producing high-quality pure iron components requires a detailed analysis of the L-PBF process, including printing

parameters and typical defects. Since the energy equations are directly related to the printing parameters under study, a thorough understanding of them was necessary. By analysing these relationships, it is possible to control the porosity and mechanical performance, ultimately improving the suitability of L-PBF pure iron for biomedical applications.

# 3. Materials and Methods

## 3.1 Scope of Experimental Work

Understanding how printing parameters and object geometry affect mechanical properties is a key focus of this study. As mentioned earlier, AM offers significant potential due to its ability to create intricate components that would be difficult or impossible to produce with conventional manufacturing methods. However, gaining insight into the various stages of the production process and the impact of different parameters on the material is essential. Since the ultimate objective of the GradImp project is to develop biodegradable porous iron implants, a thorough understanding of how each variable influences the final product is crucial to achieving an optimized and suitable implant for human use. Therefore, this project is divided into two stages: the first in which the pure iron powder is subjected to tests in order to characterize the material and the second stage in which 144 printed parts are evaluated and the aim is to study and relate the effects that the printing parameters have on the geometry of the parts and especially on their mechanical properties.

## 3.2 Overview

Subchapter 3.3 presents all the equipment and tools used throughout this project. Subchapter 3.4 describes the material used to print the parts. In Subchapters 3.5 and 3.6, all the experimental work is explained in more detail. The results and their discussion can be found in chapter 4. For a clearer understanding of the nature of this experimental work, it is recommended to review the flowchart presented below (Figure 17).

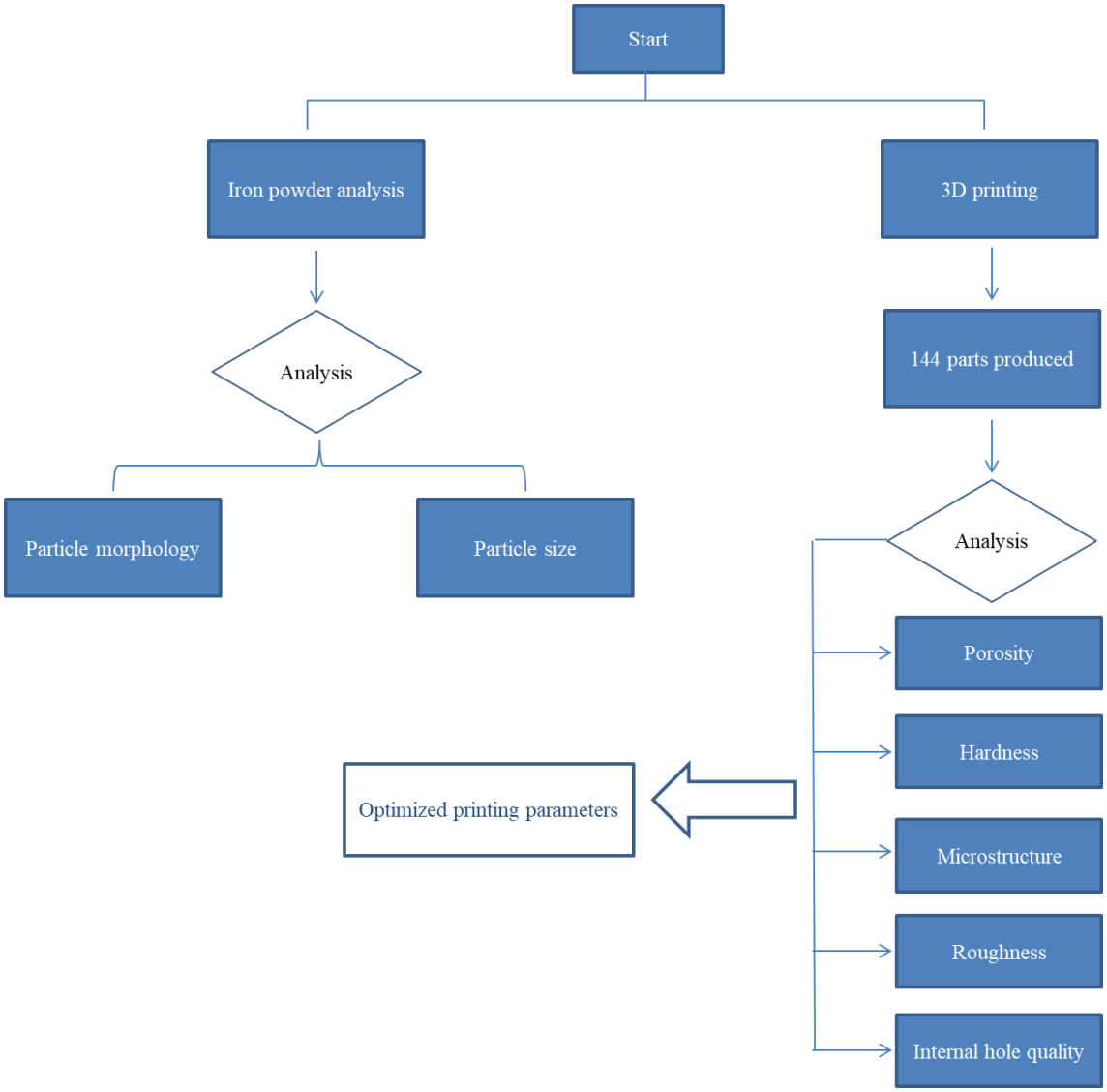


Figure 17 - Flowchart of the experimental work conducted

## 3.3 Equipments and Tools

Throughout this project, various instruments have been used to carry out these tests. They will all be mentioned below.

- **3D Printer:** To produce the different pure iron samples, the 3D printer "Concept Laser M2 Series 5" was the selected (Figure 18). This equipment is available at INEGI (Institute of Science and Innovation in Mechanical and Industrial Engineering). Table 5 shows some important specifications provided by the manufacturers for this machine.

Table 5 - Concept Laser M2 Series 5 specifications from manufacturers website [80,81]

| M2 Series 5 - Technical Data | |
|---|---|
| Technology | Laser Powder Bed Fusion (L-PBF) |
| Print volume ($mm^3$) (x,y,z) | 245 x 245 x 405 |
| Printer dimensions ($mm^3$) | 2739 x 2050 x 2781 |
| Weight (Kg) | Approx. 2500 |
| Operating conditions (°C) | 18 - 25 |
| Layer thickness (µm) | 25 - 120 |
| Laser system options (cw) | Fibre Laser 2 x 1kW<br>Fibre Laser 2 x 400W |
| Scanning speed (m/s) | Max 4,5 (with variable focus adjustment) |
| Focus diameter (µm) | 61 - 72 |
| Spot size range (µm) | 70 - 500 |

The atmosphere of the machine chamber contains an inert gas, usually argon or nitrogen (nitrogen in the case of the machine used), to prevent contamination and oxidation of the powder. A very important factor for medical applications.

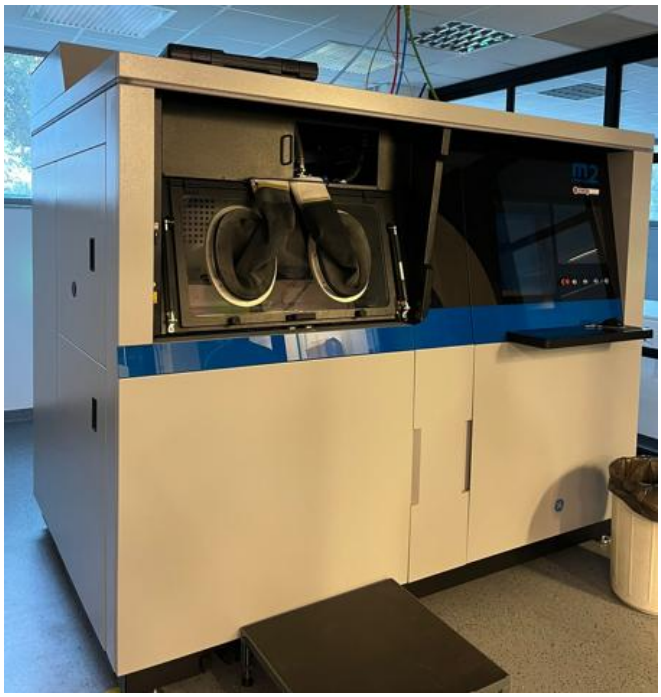

Figure 18 - Concept Laser M2 Series 5 installed in INEGI

- **Scanning Electron Microscope (SEM):** In order to do the particle morphology analysis of the iron powder, a "Phenom XL" (Figure 19) from Thermo Scientific was used. In addition, EDS (Energy Dispersive Spectroscopy) was employed to obtain compositional analysis of the powder. Table 6 shows some important specifications provided by the manufacturers for this machine.

Table 6 - Phenom XL specifications from manufacturers website [81]

| Phenom XL - Technical Data | |
|---|---|
| Electron optical magnification range | 160 - 200,000x |
| Light optical magnification | 3–16x |
| Resolution | <10 nm |
| Image resolution options | 960 x 600, 1920 x 1200, 3840 x 2400 and 7680 x 4800 pixels |
| Acceleration voltages | Default: 5 kV, 10 kV and 15 kV |
| Detector | Backscattered electron detector (standard)<br>Secondary electron detector (optional)<br>Energy-dispersive X-ray spectroscopy (EDS) detector (optional) |
| Sample size | Max. 100 mm x 100 mm (up to 36 x 12 mm pin stubs)<br>Max. 40 mm (h) |


Figure 19 - Phenom XL (at DEMec FEUP)

- **Particle Size Analyzer:** To determine the particle size of the iron powder using the digital light scattering (DLS) method, the "LS 230" from Coulter (Figure 20) was chosen. This equipment measures particles from 0,04 µm to 2000 µm.


Figure 20 - Coulter LS 230 (at DEQ FEUP)

- **Universal Milling Machine:** The printed parts were removed from the printing plate with this milling machine (Figure 21) from the manufacturer Induma.


Figure 21 - Induma milling machine (at DEMec FEUP)

- **Electric Discharge Machine:** The printed pieces were longitudinally cut for later porosity analysis with "RoboCut α-C400iC" (Figure 22) from the manufacturer FANUC.


Fig 22 - RoboCut α-C400iC (at DEMec FEUP)

- **Press Molding Machine:** The parts were applied in resin with “Prontopress-2” (Figure 23) from the manufacturer Struers.


Figure 23 - Prontopress-2 (at DEMec FEUP)

- **Grinding and Polishing Machines:** The parts previously applied in resin were grinded and polished with “RotoPol-21” (Figure 24) from the manufacturer Struers.


Figure 24 - RotoPol-21 (at DEMec FEUP)

- **Stereo Microscope:** In order to obtain images for later analyse of the characteristics of the printed parts such as hole, top surface roughness and porosity, “Olympus SZ-ET microscope” (Figure 25) from the manufacturer Olympus Europe was the machine used. It is equipped with a digital camera “Zeiss Axiocam 208 color”.


Figure 25 - Olympus SZ-ET microscope (at DEMec FEUP)

- **Microscope:** The microstructure of the printed parts was analysed with "Zeiss Axioplan 2 microscope" (Figure 26) from the manufacturer ZEISS.

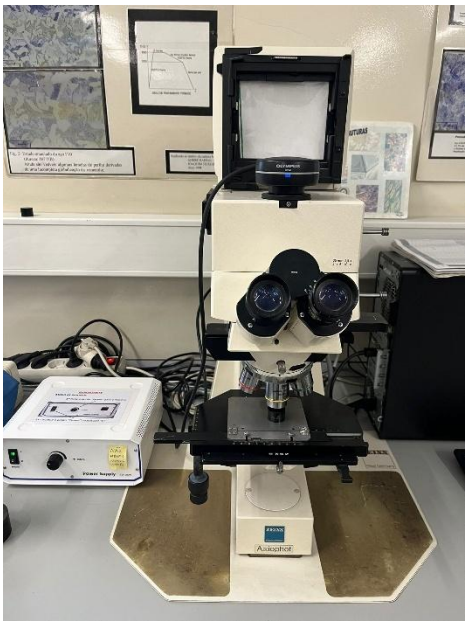

Figure 26 - Zeiss Axioplan 2 microscope (at DEMec FEUP)

- **Digital Caliper:** The height of the internal hole of the parts was measured with "Skjutmått Digital Caliper 150 mm" (Figure 27) from the manufacturer LIMIT. The resolution of the instrument is 0.01 mm.


Figure 27 - Digital caliper (at DEMec FEUP)

- **Surface Roughness Tester:** The roughness of the parts was determined with "LV-50" (Figure 28) from the manufacturer HOMMELWERKE.

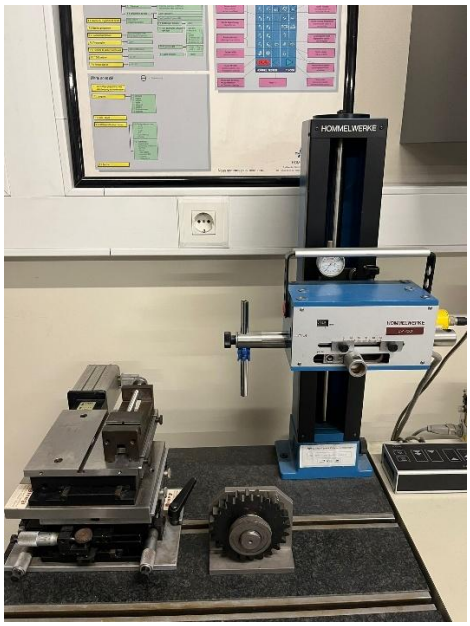


Figure 28 - LV-50 (at DEMec FEUP)

- **Hardness tester:** The Vickers hardness of the printed parts was measured using a **"**WOLPERT DIA TESTOR 2 RC" (Figure 29).

Figure 29 - WOLPERT DIA TESTOR 2 RC (at DEMec FEUP)

## 3.4 Materials

The material selected for this experimental part used in the Concept M2 Series 5 was ATOMET FeAM from manufacturer Rio Tinto, which is a high purity iron powder suitable for additive manufacturing applications. The powder was produced by the water atomization process. Figure 30 shows two SEM images of the powder provided by the supplier. Its apparent density is presented as 3.10 g/cm$^3$ [82].

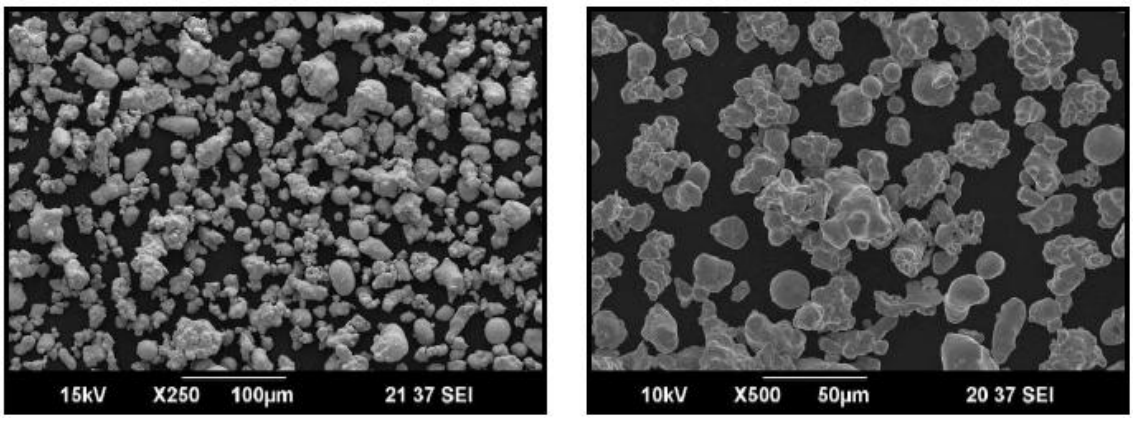


Figure 30 – SEM images of the iron powder provided by the manufacturer [82]

The chemical composition and data sheets of the material are shown in Tables 7,8,9 and 10.

Table 7 - Powder typical chemical composition [82]

| **Typical chemical composition (% by weight)** | |
|---|---|
| Iron | > 99.5 |
| Manganese | 0.04 |
| Carbon | 0.004 |
| Oxygen | 0.08 |
| Sulfur | 0.007 |
| Nitrogen | 0.004 |

Table 8 - Powder typical size distribution [82]

| **Typical particle size distribution** | |
|---|---|
| $d_{10}$ | 15 µm |
| $d_{50}$ | 30 µm |
| $d_{90}$ | 45 µm |
| $d_{99}$ | 60 µm |

The following technical data provided by the manufacturer is for information purposes only. The properties reported here were obtained by printing ATOMET FeAM with an EOSINT M 280 printing machine (powder-bed selective laser melting) with optimised process parameters [82].

Table 9 - General process data [82]

| **General process data** | |
|---|---|
| Typical achievable part accuracy (small part < 80 x 80 mm)[1] | Approx. ± 30 µm |
| Minimal wall thickness | Approx. 0.2 mm |
| Surface roughness (as manufactured)<br>- Layer plane (xy)<br>- Build direction (z) | <br>Ra 4 µm (0°)<br>Ra 8 µm (90°) |
| Surface roughness (after shot-peening)<br>- Layer plane (xy)<br>- Build direction (z) | <br>Ra 5 µm (0°)<br>Ra 5 µm (90°) |
| Volume rate (total build speed including recoating) | 8 $cm^3/h$ |
| Achievable density | 7.80+ $g/cm^3$ |

Table 10 - Mechanical properties [82]

| **Mechanical properties** | **As-build** | **Stress-relieved[2]** |
|---|---|---|
| Yield strength<br>- Layer plane (xy)<br>- Build direction (z) | <br>550 MPa<br>450 MPa | <br>460 MPa<br>450 MPa |
| Tensile strength<br>- Layer plane (xy)<br>- Build direction (z) | <br>600 MPa<br>500 MPa | <br>510 MPa<br>490 MPa |
| Elongation strength<br>- Layer plane (xy)<br>- Build direction (z) | <br>Approx. 13%<br>Approx. 13% | <br>Approx. 19%<br>Approx. 16% |
| Modulus of elasticity<br>- Layer plane (xy)<br>- Build direction (z) | Typ. 210 GPa | |

[1] Following a standard EOS calibration procedure (optimised beam-offset).

[2] Stress-relief heat treatment : 30 minutes at 600°C.

## 3.5 Iron powder analysis

In order to characterize the iron powder used in the 3D printing process, several tests were carried out in laboratory to obtain relevant information about the shape, morphology and particle size of this metal. These tests are useful for assessing the quality of the powder and comparing it with the data provided by the supplier. The iron powder used throughout this project can be seen in Figure 31.

Figure 31 - Iron powder used throughout this project

### 3.5.1 Particle morphology analysis

SEM is an essential instrument for analysing particle's morphology, size, shape, and surface structure in the context of powder analysis. Depending on sample preparation and equipment parameters it is possible to obtain 3D images which offer topographical details. In addition, by employing EDS (Energy Dispersive Spectroscopy), it is possible to obtain compositional analysis, i.e. information about the chemical composition of the powder.

Some SEM images were taken at two different magnifications. However, for a more reliable analysis, four images at the same magnification (1000x) were used. The accelerating voltage applied to the electron beam was 15V, a high value due to the good

conductivity of iron, which allows for better contrast and greater depth of field, as well as greater penetration of the electron beam. It should also be noted that the SEM microscope operates under vacuum so that the electron beam is not scattered by air particles, thus guaranteeing a sharper image.

In order to analyse the shape and morphology of the particles, SEM analysis was then carried out on the "Phenom XL" machine. After taking the SEM images, they were then loaded into imageJ software (version 1.54k), where they were segmented (thresholded) to highlight the particles and then measure their properties. This data was then transferred in column form to Excel software (version 2501) for later analysis. The two properties that stood out as most relevant in order to analyse the morphology of the particles are circularity, which can be understood as a measure of the similarity of the particle to a sphere, and aspect ratio, which is the ratio of the length (longest axis) to the width (shortest axis) of a particle.

- The circularity scale goes from 1 (completely circular) to 0 (very elongated or irregular). A rough particle surface leads to low numerical values of the parameter circularity. ImageJ uses the formula in Eq. (5) to determine circularity:

$$Circularity = \frac{4 * \pi * Area}{Perimeter^2} \quad (5)$$

- Aspect ratio expresses the particle's length or stretch. A perfect circular shape is represented by the number 1, whilst longer shapes are represented by larger values. ImageJ uses the formula in Eq. (6) to determine aspect ratio:

$$Aspect\ Ratio = \frac{Longest\ axis}{Shortest\ axis} \quad (6)$$

### 3.5.2 Particle size analysis

Digital light scattering (DLS), sometimes called dynamic light scattering, gives a hydrodynamic size, which is a measurement of the behaviour of the particles in solution

that also accounts for the influence of surrounding liquid molecules. A sample of the iron powder was then subjected to this method of analysis in “LS 230” machine and the results transcribed into a text file for later analysis.

## 3.6 3D printing

This dissertation is a follow-up to a previously started project, in which there had already been two preliminary prints with simpler geometries (cubes). In the first print, we tried to visibly identify the parts that had been undermelted and overmelted. In the second impression, a more in-depth porosity analysis was carried out. To do this, the pieces were cut crosswise and the set of parameters that resulted in pieces with porosity of less than 1% was identified. Using the optimized process windows found in the previous prints, a more focused analysis was carried out in this experiment with 144 additional parts. The parameters used for this experiment are listed in Table 11.

The geometry of these parts is much more sophisticated compared to previous printing (cubes). It was chosen to introduce the number of each part on one of the side faces, an internal hole in the shape of an arc and a 45º exit angle that connects the part to the printing plate (Figure 32). Figure 33 shows the technical drawing of the part, where the dimensions are in mm. In this print, a more complex geometry was modeled to evaluate the ability of different parameter variations to print more sensitive regions, namely a horizontal hole without supports and 45º protrusions. This is the angle because all the geometries modeled in the future have this inclination. The parts were removed from the printing plate using an Induma universal milling machine. The parts were then subjected to various tests, which are explained in the following subchapters.

Table 11 - Pure iron L-PBF parameters tested in this 3D printing

| Scanning Speed (mm/s) | Spot Size (µm) | Hatch Spacing (mm) |
|---|---|---|
| 500 | 110 - 170 step: 20 | 0,16 - 0,21 step: 0,01 |
| 600 | | 0,135 - 0,185 step: 0,01 |
| 700 | | 0,115 - 0,165 step: 0,01 |
| 800 | | 0,1 - 0,15 step: 0,01 |
| 900 | | 0,09 - 0,14 step: 0,01 |
| 1000 | | 0,08 - 0,13 step: 0,01 |

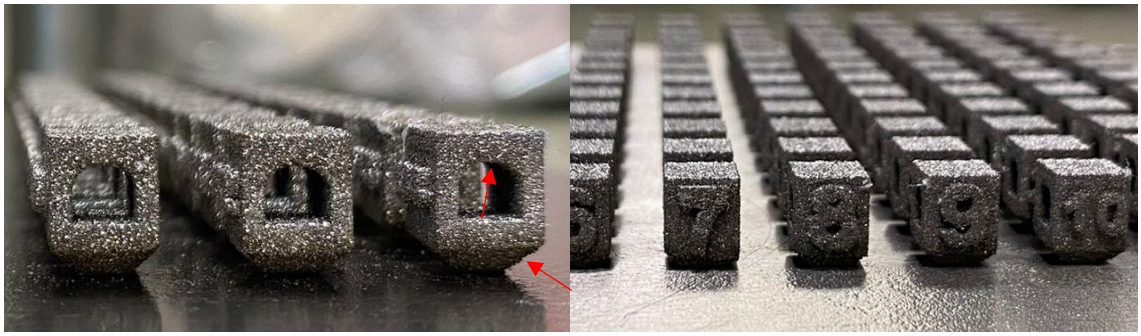

Figure 32 - Internal arc and 45º angle (left); part number on side face (right)

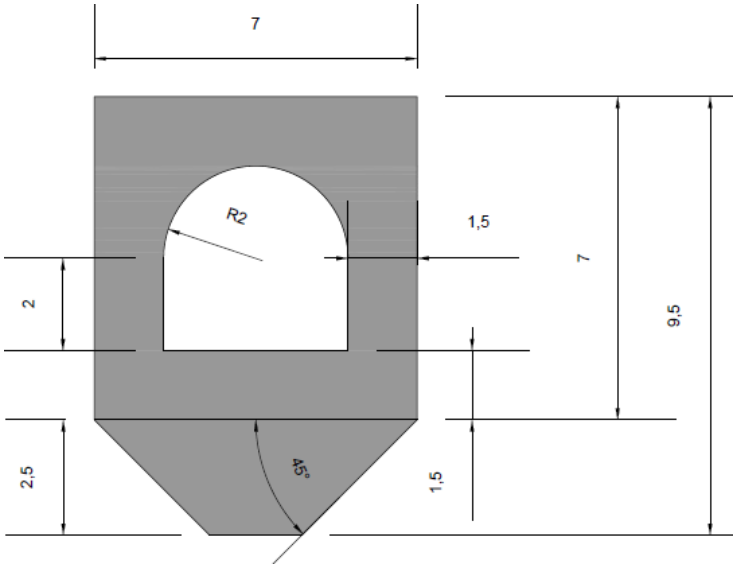


Figure 33 - Technical drawing of the part (dimensions in mm)

### 3.6.1 Porosity measurements

Since this print was based on the optimized process windows identified in the previous print, it would make sense to also analyse the porosity of the new parts. Also, to understand how the more complex geometry of the new part influences this porosity and, consequently, its relative density, a very important factor for biomedical applications. However, it should be noted that in this print, the cut was longitudinal, whereas in the previous print it was transversal.

In order to assess the porosity of the parts, the pieces were cut longitudinally using electrical discharge machining with the use of a FANUC RoboCut α-C400iC machine. Once the longitudinally cut parts had been obtained, they were then placed in resin (EpoMet F 20-3381-160) on Prontopress-2 machine and then polished with 320 and 800 grit silicon carbide sandpaper on ProtoPol-21 machine. Polishing cloths impregnated with 3 μm and 1 μm suspended diamonds were then used. Using an Olympus SZ-ET microscope, images of the pieces were captured at 12x magnification with software ZEN 3.3 (blue edition) and their porosity was determined using ImageJ software.

After obtaining the porosity values for each piece, the influence of different printing parameters on porosity was analysed. This was done using graphs that related the various variables.

This analysis is very important in order to continue with the method of tapering printing parameters until the optimum ranges are reached.

### 3.6.2 Hardness measurements

To determine the hardness, all 144 parts were subjected to this test. The test was carried out on the WOLPERT DIA TESTOR 2 RC hardness tester. Once the average value has been obtained, the tabulated values are consulted and the Vickers hardness value is extracted. It should be noted that this procedure was repeated three times for each part in order to obtain a reliable average hardness value.

After obtaining the hardness values for each piece, the influence of different printing parameters on hardness was analysed. This was done using graphs that related the various variables.

### 3.6.3 Microstructure analysis

A microstructural analysis of the printed parts was considered relevant to the study. For this purpose, one of the parts with the most promising results was chosen. Part number 108, out of a total of 144 parts, which has low porosity and high hardness, was chosen. Table 12 shows the characteristics of the part, as well as the printing parameters that gave rise to it. It should be noted that, as with any other part, the laser power and layer height values were 300 W and 50 µm, respectively.

Table 12 - Characteristics of the analysed part

| Scanning Speed (mm/s) | Spot Size (µm) | Hatch Spacing (mm) | Energy Density J/mm3 | Energy Intensity J/mm2 | Porosity (%) | Hardness (HV) |
|---|---|---|---|---|---|---|
| 800 | 130 | 0.15 | 50 | 22601.89 | 0.37 | 157.75 |

To carry out this analysis, the piece was again polished on diamond sandpaper at a speed of 150 rpm and then attacked with 2% Nital. This attack was repeated a few times until the part's microstructure was revealed. The part was then observed using a Zeiss Axioplan 2 microscope and images were captured for later evaluation.

### 3.6.4 Influence of printing parameters on final part quality

One of the aspects that was considered important to evaluate was the direct influence that each printing parameter has on the final result of the pieces. The parameters in question are scanning speed, spot size and hatch spacing. Whereas energy density and energy intensity are also criteria to be taken into account, since they are implicit as they relate to all the parameters mentioned above. The influence of the parameters laser power and laser height were not analysed individually, since they were constant values for all printed parts. As such, small samples of parts were selected from the 144 available in which the difference within each sample was the change in the values of one printing parameter, while the rest remained constant. The characteristic analysed and compared was the roughness of the upper face of the parts.

In addition, a study of the dimensional accuracy of the inner hole in the part was carried out. To do this, the hole height (middle of the arch to the base of the hole) was measured using the digital caliper and its values recorded in an Excel file. Figure 34 presents the measured distance (represented by the orange arrow). Note that these values are the average of three measurements. MATLAB was used to analyse the results and generate a contour plot of hole height as a function of energy density and energy intensity, allowing for visual identification of the optimal processing windows within the tested parameters.

Initially, it was also intended to evaluate the part's exit angle, i.e. the angle that connects the base of the cube with the printing plate, but when the parts were extracted, this angle was damaged, so it was not possible to carry out this analysis.

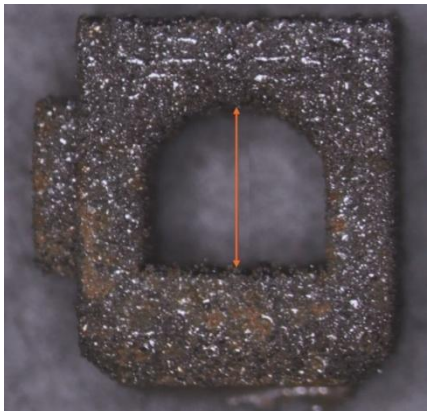

Figure 34 - Measured distance (hole height)

### 3.6.5 Roughness measurements

In order to assess the roughness of the upper face of the parts, the "LV-50" machine was selected. On this machine, roughness was measured using the contact method instead of the optical method. Although the latter is a much less invasive method for the part, much faster and capable of generating a 3D map of the surface, it could not be the method selected, since most of the parts have a medium/high roughness, with deep peaks and valleys, which could generate shading, i.e. the light would not be able to reach certain regions.

It should be noted that for each piece, three roughness measurements were taken on the top face in the longitudinal direction and another three measurements in the transverse direction. This data is then processed to calculate the roughness parameters, namely Ra (average roughness). The initial idea was to measure the roughness of all 144 pieces, but it immediately became clear that this would not be possible, as it is a very time-consuming and expensive process. As such, pieces with different roughness visible to the naked eye were chosen. One with very high roughness, one with low roughness and one with low/intermediate roughness, in order to draw some conclusions for the rest of the sample.

# 4. Analysis and Discussion

This chapter will analyse all the work done in chapter 3, discussing the results obtained.

## 4.1 Iron powder analysis

### 4.1.1 Particle morphology analysis

Figures 35 and 36 show the SEM images obtained using the Phenom XL machine.

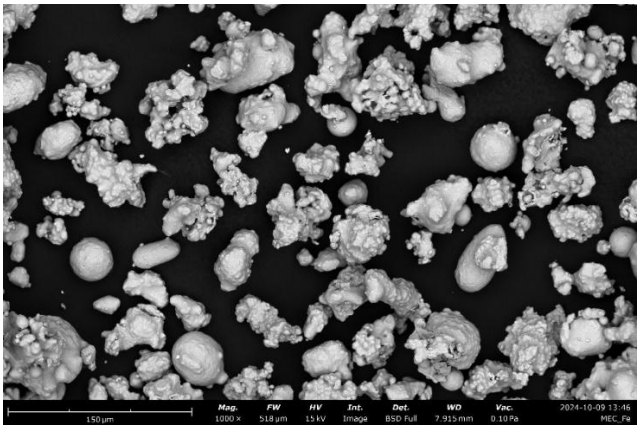


Figure 35 - Image 1 SEM of iron powder

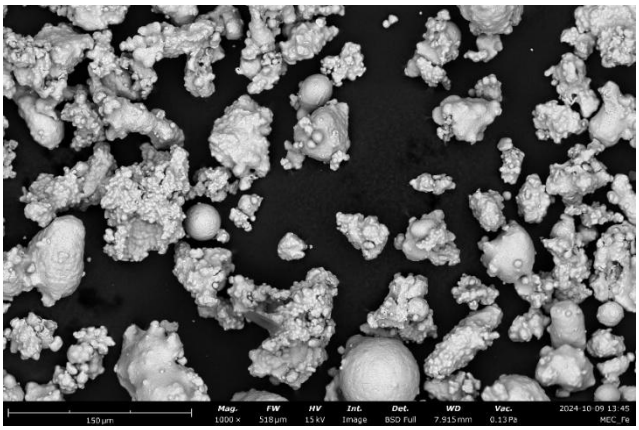


Figure 36 - Image 2 SEM of iron powder

As the images represent different regions, it makes sense to compare the results in a consolidated way to get an overview of the shape of the particles. Bar charts were created to combine the information from the different images. The circularity and aspect ratio distributions for all the particles in the sample are shown by the histograms in Figures 37 and 38, respectively.

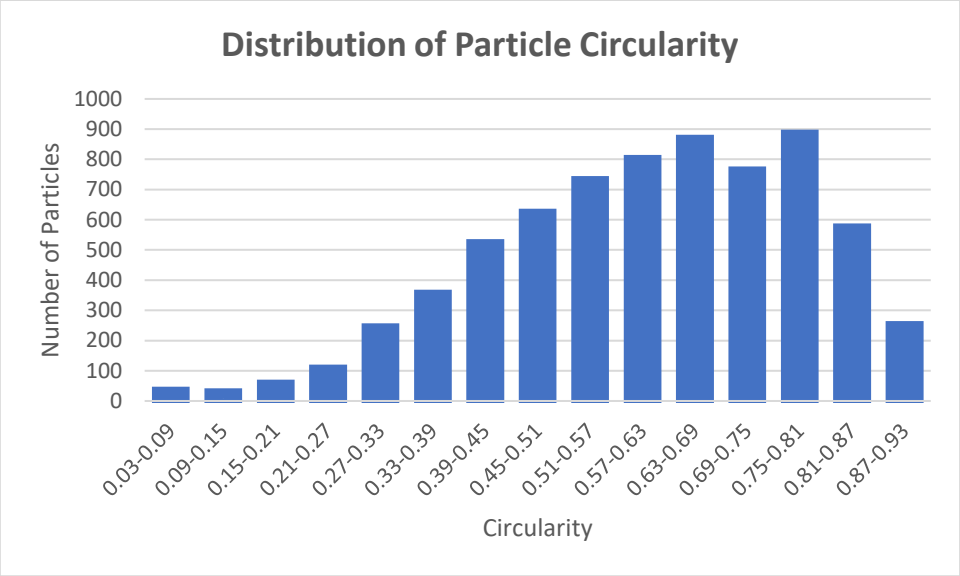


Figure 37 - Distribution of particle circularity

It is helpful to compute certain descriptive statistics for circularity and aspect ratio, such as the mean, standard deviation and median, in addition to the bar charts. The data on Tables 13 and 14 show how they differ in shape as well as a quantitative understanding of particles' average shape.

Table 13 - Circularity statistics

| Circularity statistics | |
|---|---|
| Average | 0,613 |
| Standard deviation | 0,166 |
| Median | 0,627 |

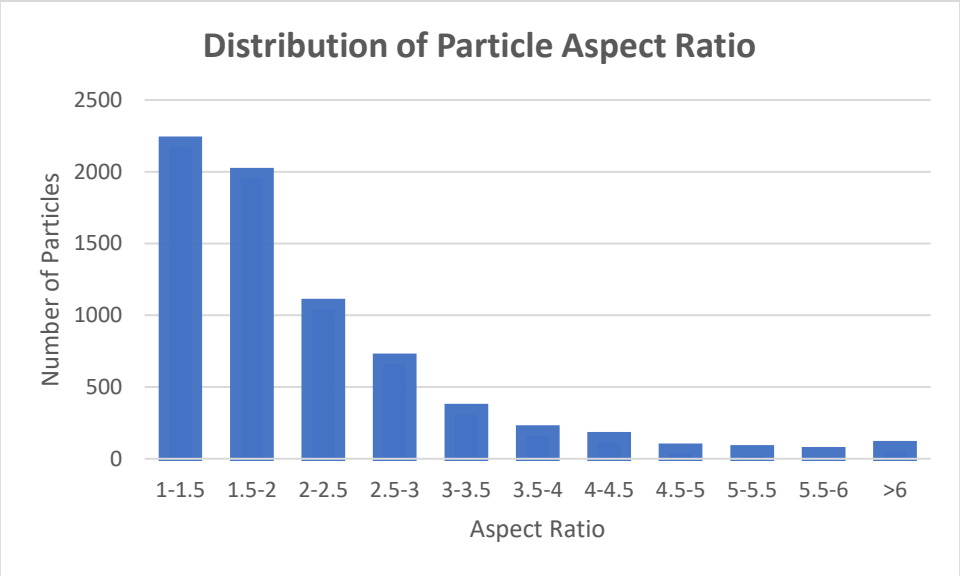


Figure 38 - Distribution of particle aspect ratio

Table 14 - Aspect ratio statistics

| Aspect ratio statistics | |
|---|---|
| Average | 2,032 |
| Standard deviation | 1,576 |
| Median | 1,724 |

After analysing the circularity and aspect ratio statistics, it can be concluded that the average is around 0,62 and 2,03, respectively. These values shows that there is a large percentage of particles that are more irregular in shape, i.e. further away from a perfect sphere. These results are in line with what can be seen in figures 31 and 32, where it is possible to see a sample with irregular particles and several aggregated satellites. These are typical characteristics of the water atomization method, as seen in the literature review in figure 6 b). The manufacturer of the powder corroborates these statements, since the powder's technical data sheet states that this is indeed the method used to produce this material [82].

For the same sample, during the microscopic analysis, EDS allowed to identify the chemical composition of the powder which, as expected, is basically iron, which corroborates the purity of the metal and the absence of oxidation. The percentage of iron present was over 99.5%. The rest was divided among the elements manganese, carbon, oxygen, sulphur, etc.

### 4.1.2 Particle size analysis

The graph presented in Figure 39 shows the particle size distribution.

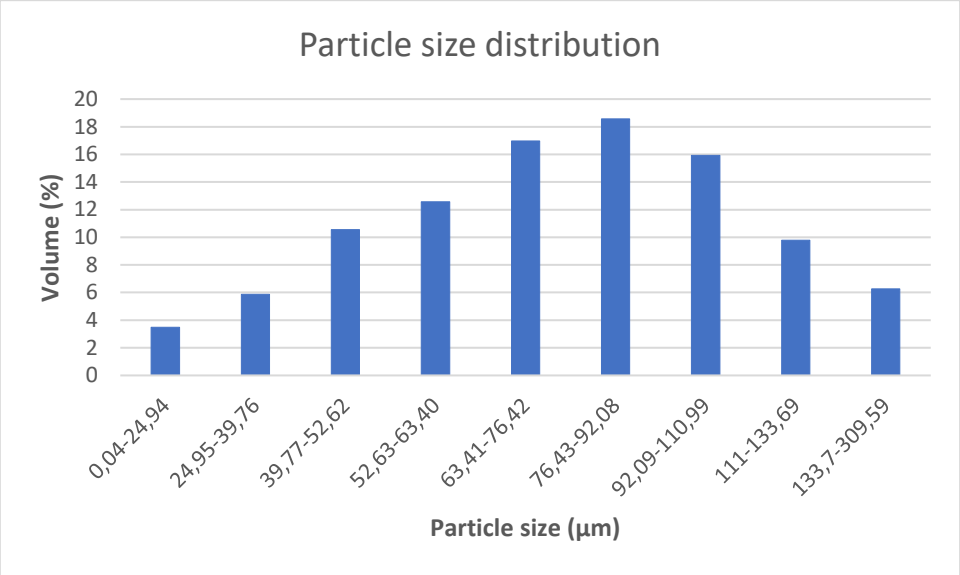


Figure 39 - Particle size distribution

Other interesting data from this particle size analysis is presented in Table 15, in order to better understand its distribution.

Table 15 - Particle size statistics

| | |
|---|---|
| Average | 80,32 µm |
| Standard Deviation | 35,60 µm |
| Median | 76,88 µm |
| d10 | 40,74 µm |
| d50 | 76,88 µm |
| d90 | 122,70 µm |
| Coefficient of Variation | 44,32% |
| Skewness | 1,023 |

After analysing this statistical data on particle size distribution, it can be said that the average particle size is 80,32 µm with a standard deviation of 35,60. The high value of coefficient of variation (44,32%) and positive asymmetry (skewness of 1,023) indicate a broad distribution, with many small particles and some larger ones, i.e. there is a considerable variation in particle size.

The fact that this is not a uniform distribution could be a negative factor when 3D printing this metal powder, as it could make it difficult to form a uniform, dense powder layer when printing. It can also increase unwanted porosity in the final product.

Table 16 compares the values obtained experimentally with those supplied by the manufacturer (Rio Tinto) for the percentile distribution of particle size.

Table 16 - Comparison of values of particle size distribution

| | Experimental values | Theoretical values |
|---|---|---|
| d10 | 40,74 µm | 15 µm |
| d50 | 76,88 µm | 30 µm |
| d90 | 122,70 µm | 45 µm |

The values obtained experimentally are much higher than those announced by the manufacturer Rio Tinto and there are several possible reasons for this. Over time, iron powder particles can aggregate or form agglomerates due to humidity, oxidation or electrostatic interactions. This increases the apparent size of the particles measured. In addition, the manufacturer's analysis may have included measures to disperse the particles, which would have decreased aggregation.

However, the results might not accurately represent the distribution if a heterogeneous sample was used. The d10, d50, and d90 values provided by the manufacturer might be an idealized distribution or average that was produced under carefully monitored conditions and might not accurately reflect variability in the real world. Manufacturers may also use trimmed data (excluding outliers) or normalized distributions to present the powder as having a narrower size range.

## 4.2 3D printing

This section details the results and respective critical analyses of the printed pieces, always trying to relate them to the printing parameters.

### 4.2.1 Influence of printing parameters on porosity

Porosity is one of the most important aspects, if not the most important, to analyse. This is because, first and foremost, the part has to be as dense as possible, which will give it the lowest possible porosity, ideally close to 0%.

To this end, initially it was studied how each printing parameter influences porosity. The graph presented in Figure 40 shows the relationship between scanning speed and porosity.

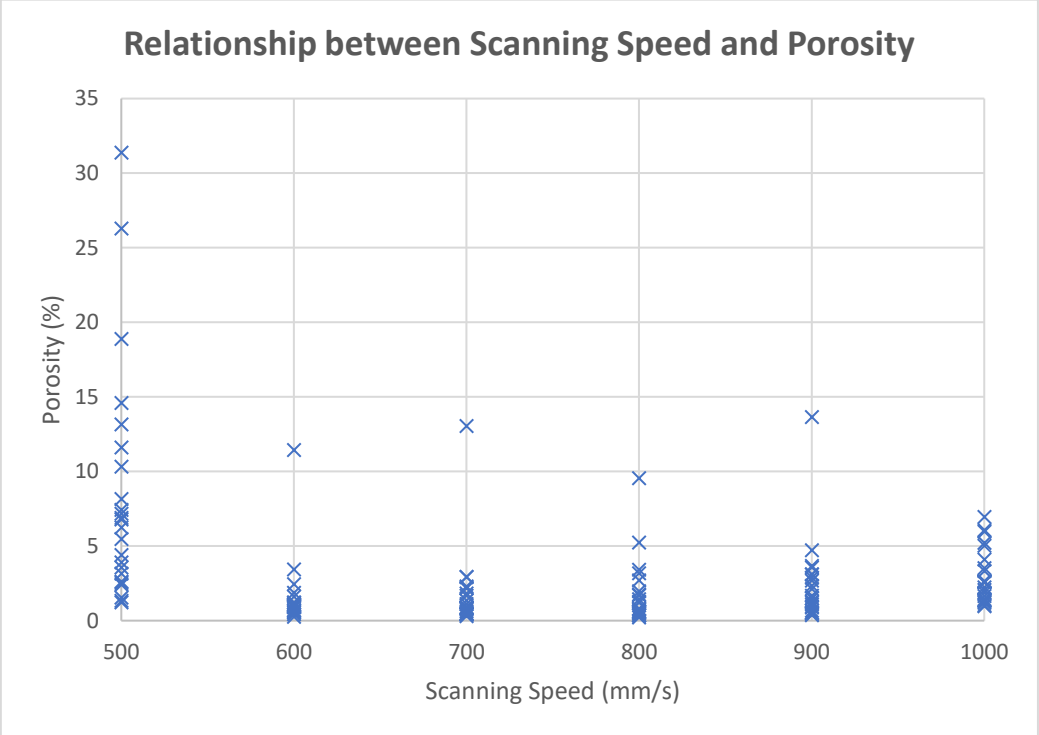


Figure 40 - Relationship between Scanning Speed and Porosity

After analysing the graph, it is clear that the lowest speed (500 mm/s) induced the greatest porosity in the parts. Lower speeds generate greater heat input into the parts, due to the excess energy deposited, which can lead to the formation of unstable cavities (porosity). As the speed increases, between 600 and 800 mm/s, porosity achieves the best results, reaching its minimum values. As the speed continues to increase up to 1000 mm/s, porosity increases again because at very high speeds, the laser moves so quickly that there isn't enough time for the material to fully melt and fuse due to the reduced energy input [83]. Figure 41 shows one part produced at 500 mm/s (left) and one part produced at 800 mm/s (right).

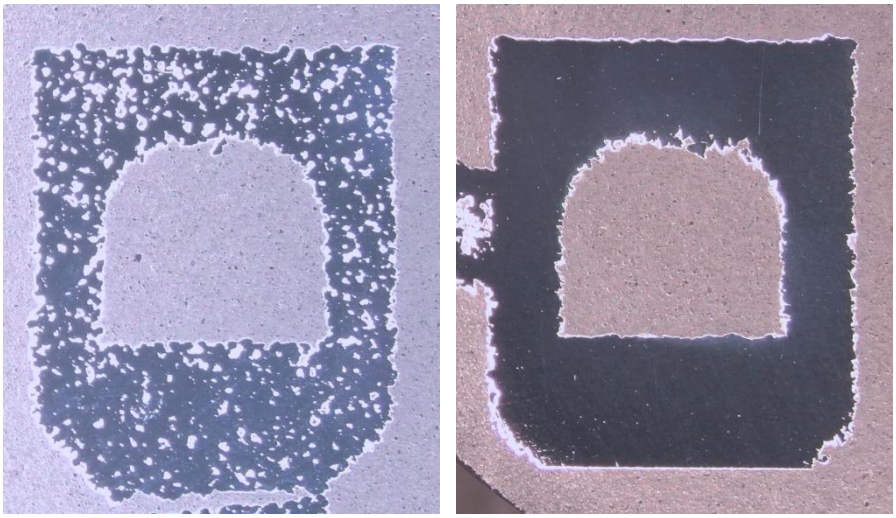

Figure 41 - Scanning speed effect on porosity

The graph presented in Figure 42 shows the relationship between spot size and porosity.

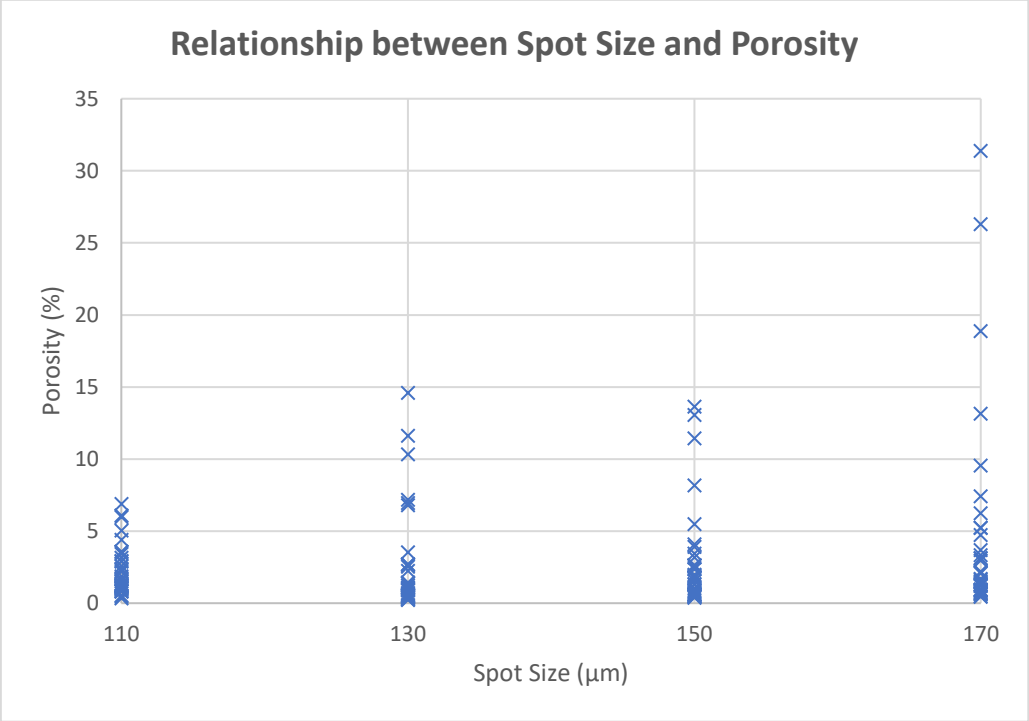


Figure 42 - Relationship between Spot Size and Porosity

It is possible to relate the increase in spot size to the increase in porosity. The pieces with the highest porosity values have in common the maximum spot size value for this study (170 µm). This can be explained by the fact that the size of the beam directly influences the distribution of energy and the dynamics of fusion. A larger spot size means that the same laser power is distributed over a larger area. This can reduce the energy intensity, resulting in incomplete fusion and porosity formation due to lack of fusion.

Regarding the hatch spacing and energy density parameters, it was not possible to find a direct relationship between them and their influence on porosity.

In order to analyse the influence of the parameters as a whole and to find the optimum window of these parameters that results in parts with porosity of less than 1%, the contour plot in Figure 43 shows the porosity of the 144 parts as a function of energy density and energy intensity. Note that the yellow areas on the graph may represent parts with porosity greater than 2%.

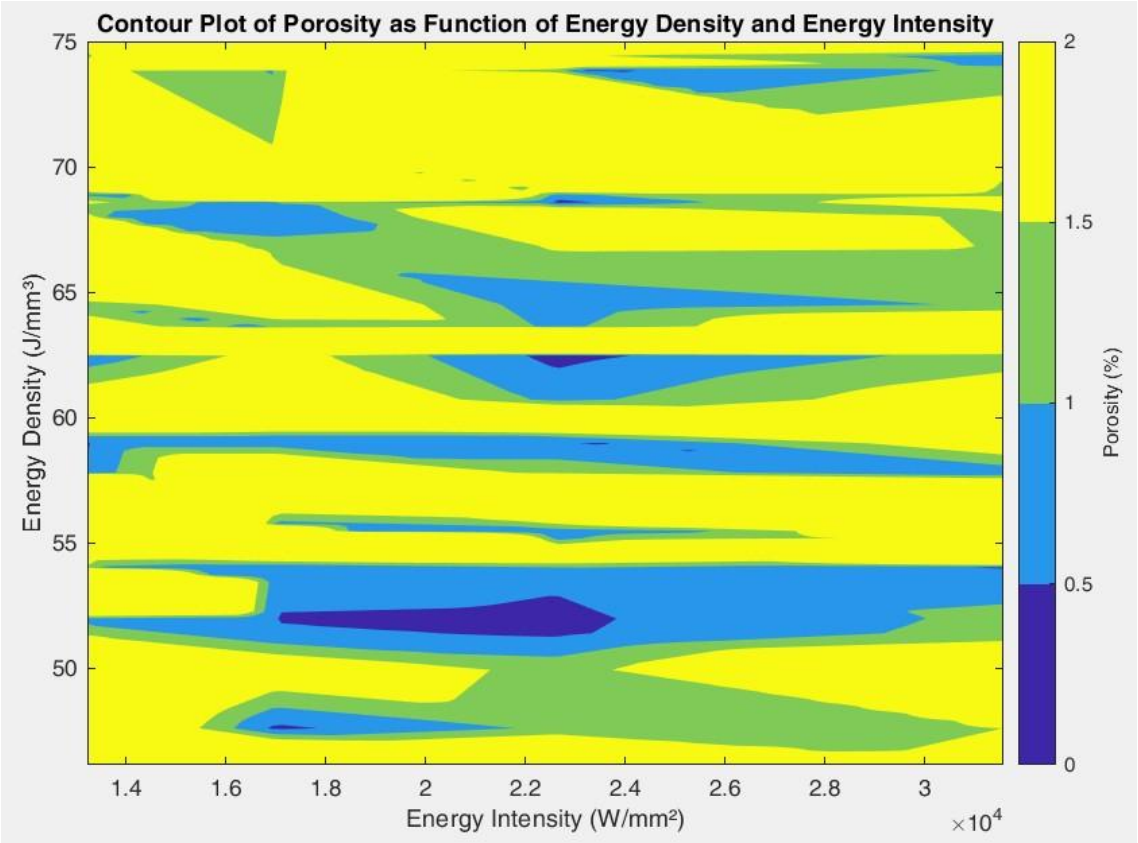


Figure 43 - Contour plot of Porosity as function of Energy Density (J/mm³) and Energy Intensity (W/mm²)

After an analysis of the contour plot, it can be seen that there are several regions of the graph that represent parts whose density is greater than 99%, i.e. parts whose porosity is less than 1%. The region that stands out the most is undoubtedly the one between 51 and 54 J/mm$^3$ of energy density. It should be noted that there are good results for any energy intensity value, which proves that spot size is not a determining factor in obtaining parts with high density. In addition to this region, there are also two areas that stand out, those between 58 and 63 J/mm$^3$.

### 4.2.2 Influence of printing parameters on hardness

The statistics of the hardness tests carried out on the 144 parts are shown in Table 17:

Table 17 - Hardness statistics

| | |
|---|---|
| Average (HV) | 149 HV |
| Standard Deviation (HV) | 7.57 HV |
| Median (HV) | 148 HV |
| Coefficient of Variation | 5.07 % |
| Min Value (HV) | 116 |
| Max Value (HV) | 168 |

These results are promising in that they correspond to the hardness obtained by other studies carried out on pure iron made by this 3D printing method with similar printing parameters, such as the work of Palousek et al. [84] and Pavel Lejcek et al. [85].

One of the major concerns in this field of study is the mechanical properties conferred on pure iron parts by this printing method. Above all, for this material to be a good candidate for a bone implant, it needs to have good properties, especially very high density, which gives the parts as little porosity as possible [86], and considerable hardness so that the implant doesn't suffer from premature corrosion or mechanical failure [83]. For this purpose, an acceptable hardness is considered to be above 145 HV [84,85]. The contour plot in Figure 44 shows the hardness of the parts as a function of energy density and energy intensity. These parameters, as has already been mentioned several times, include all the variable printing parameters.

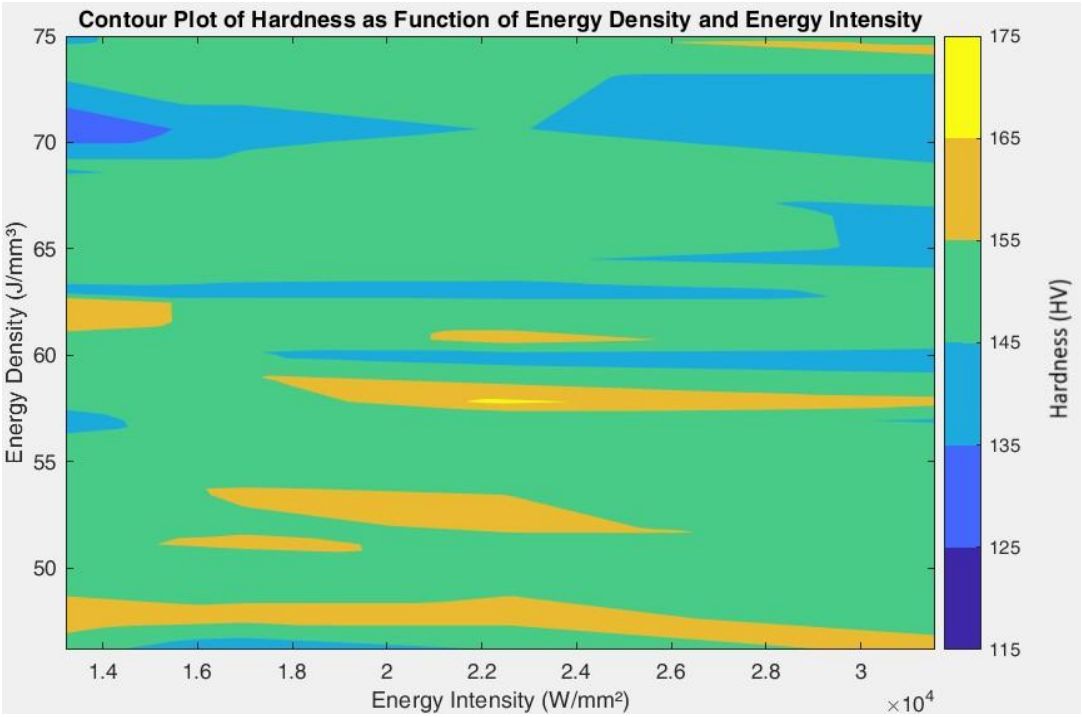


Figure 44 - Contour plot of Hardness as function of Energy Density (J/mm³) and Energy Intensity (W/mm²)

Analysis of the contour plot shows that most of the parts resulted in a hardness of over 145 HV, specifically 83.45%. These hardness values are recorded mainly for the energy density range between 45 and 59 J/mm$^3$. As far as energy intensity is concerned, this is not a factor that has a significant influence on the density of the parts, so consequently neither is the spot size parameter.

As the energy density is the most influential factor, attention is focused on the scanning speed and hatch spacing parameters [87]. The latter did not reveal a pattern of direct influence on hardness. However, an interesting conclusion can be drawn from the graph relating the scanning speed parameter to hardness. The graph is shown in Figure 45.

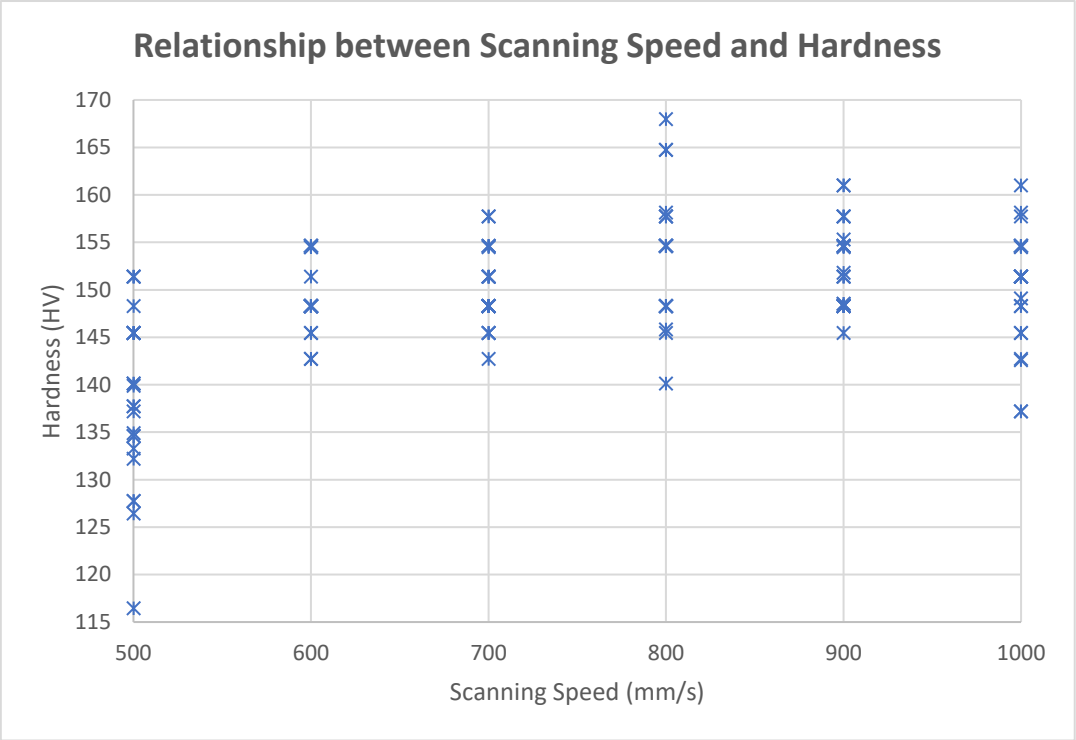


Figure 45 - Relationship between Scanning Speed and Hardness

It can be seen that the lowest hardness values are associated with the lowest speed (500 mm/s). As the speed increases, the hardness also tends to increase until it reaches its maximum value of 168 HV for a speed of 800 mm/s. As the speed continues to increase, the hardness decreases slightly, but almost always remains higher than 145 HV.

As mentioned earlier, the mechanical properties density and hardness are highly impacted by the porosity of the parts [88]. The graph in Figure 46 shows the relationship between hardness and porosity.

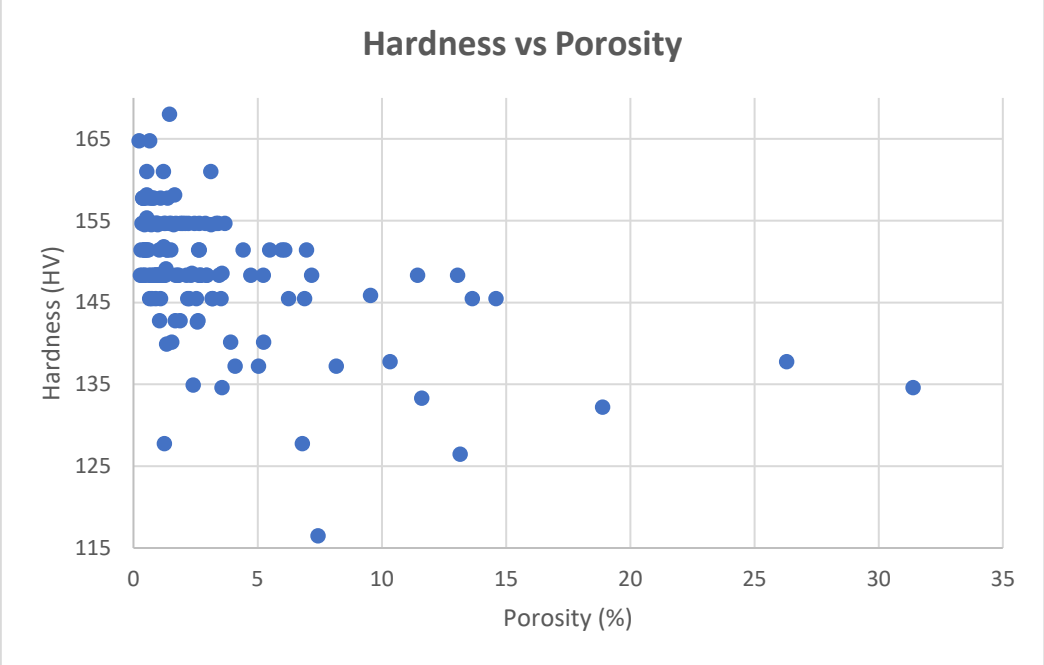


Figure 46 - Relationship between Hardness and Porosity

Although there is no linear relationship between the two quantities, it should be noted that the parts with the highest hardness are also the parts with the lowest porosity. This makes sense, since parts with lower porosity tend to have more compact and resistant structures, with fewer pores, which leads to a higher hardness value.

Since these are the most important characteristics to take into account, it is advisable to analyse the two contour plots depicted in Figures 43 and 44. The best candidates for bone implants will then be the parts that correspond to the optimum region of the overlap between the two contour plots. Therefore, the parts with the best mechanical properties, essential for implementation in the biomedical field, are those whose energy density is between 51-54 J/mm$^3$ and 58-63 J/mm$^3$.

### 4.2.3 Microstructure results

Figures 47 and 48 show the microstructure of part number 108 at 10x and 20x magnification, respectively.

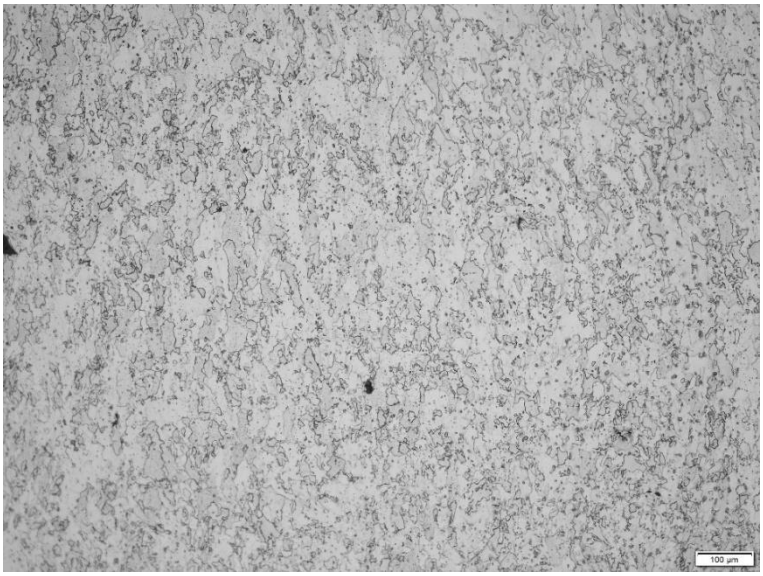


Figure 47 - Microscope image, 10x magnification

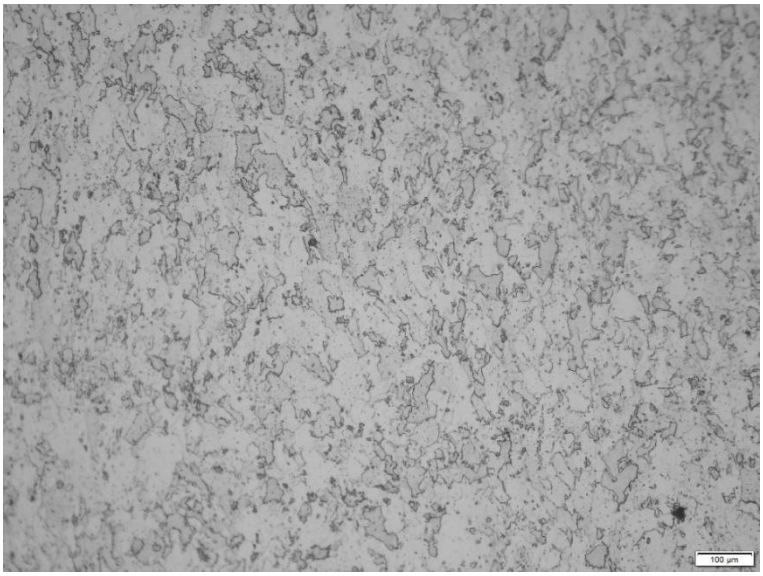


Figure 48 - Microscope image, 20x magnification

The microstructure of the pure iron part produced by the L-PBF process is composed of coarser and finer grains with distinct grain boundaries. A characteristic of

materials processed by this method is the random arrangement of the grains, something that can be clearly seen in these two images. The microstructure is not homogeneous; grain sizes vary considerably. Furthermore, there is no discernible transition between successive printing layers. The black dots in the images indicate microporosity, where the larger irregularly-shaped dots resemble a type of porosity called keyhole and the smaller circular dots are the result of trapped gases. They could also be oxide inclusions. These results are considered satisfactory as they are in line with the study carried out by David Palousek et al. [84] where they present very similar results in terms of microstructure for pure iron parts produced by the selective laser melting (SLM) process.

### 4.2.4 Influence of printing parameters on the dimensional accuracy of the inner hole

The graphs relating the different printing parameters to the dimensional accuracy of the inner hole are shown below. The first graph is shown in Figure 49 and presents the influence that the spot size has on the hole height.

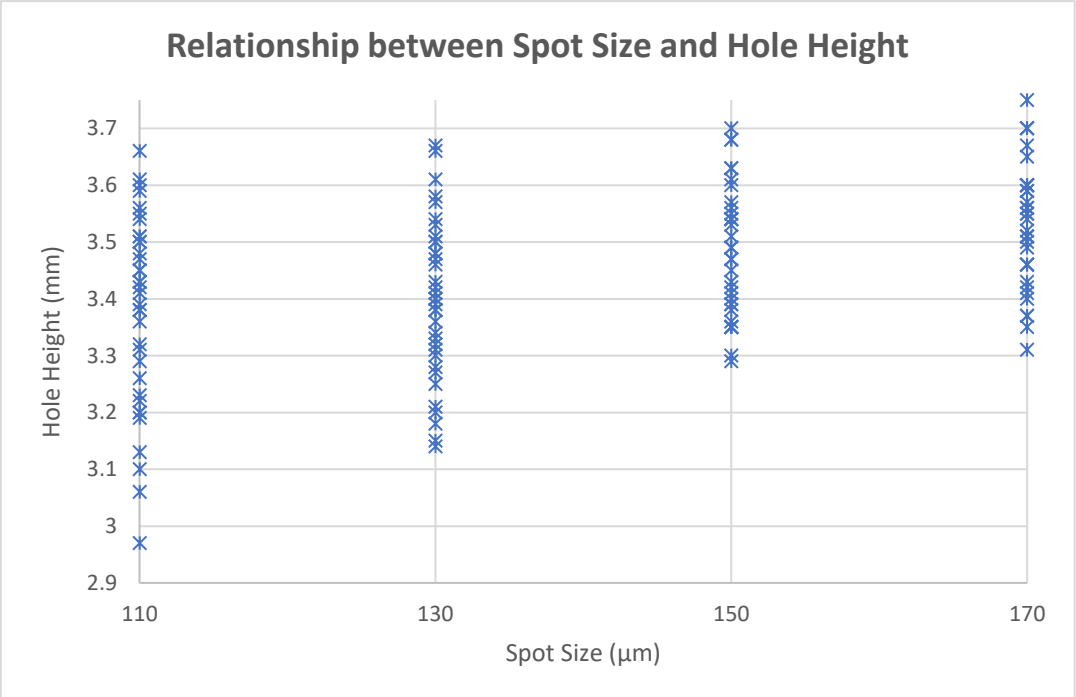


Figure 49 - Relationship between Spot Size and Hole Height

Analysis of the graph shows that as the spot size increases there is a tendency for the height of the internal hole to approach the designed value (4 mm). According to the energy intensity equation (2), which relates laser power with spot size, this improved dimensional accuracy with increasing spot size indicates that the parts with the best results are those produced with a lower energy intensity. This is due to the fact that a larger spot size for the same power results in less localized and smoother melting, with less risk of effects such as balling or excessive melting at the edges.

The graph shown in Figure 50 shows the influence that the hatch spacing has on the hole height.

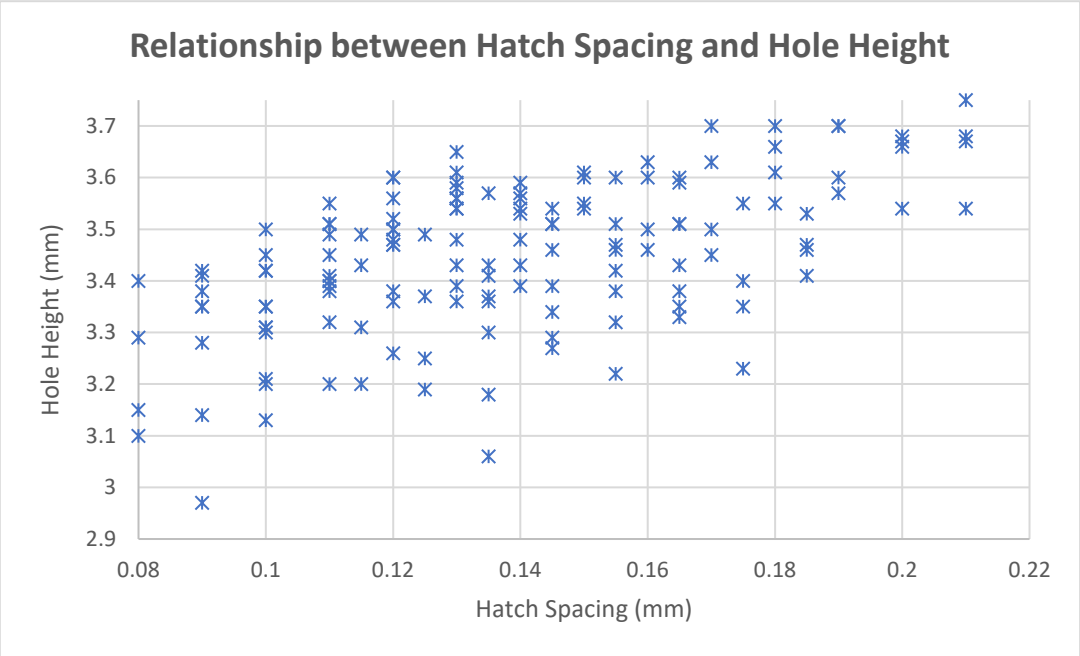


Figure 50 - Relationship between Hatch Spacing and Hole Height

After analysing the graph, it should be noted that, in general, the hole height increases as the hatch spacing value increases. According to the VED equation (1), this implies that the best results are associated with a lower energy density. This can be explained by the more homogeneous and less overlapping way in which the heat is distributed, reducing the risk of generating multiple fusion regions, which end up creating small protrusions of accumulated dust that obstruct the hole.

The contour plot shown in Figure 51 gives the hole height as a function of energy density and energy intensity.

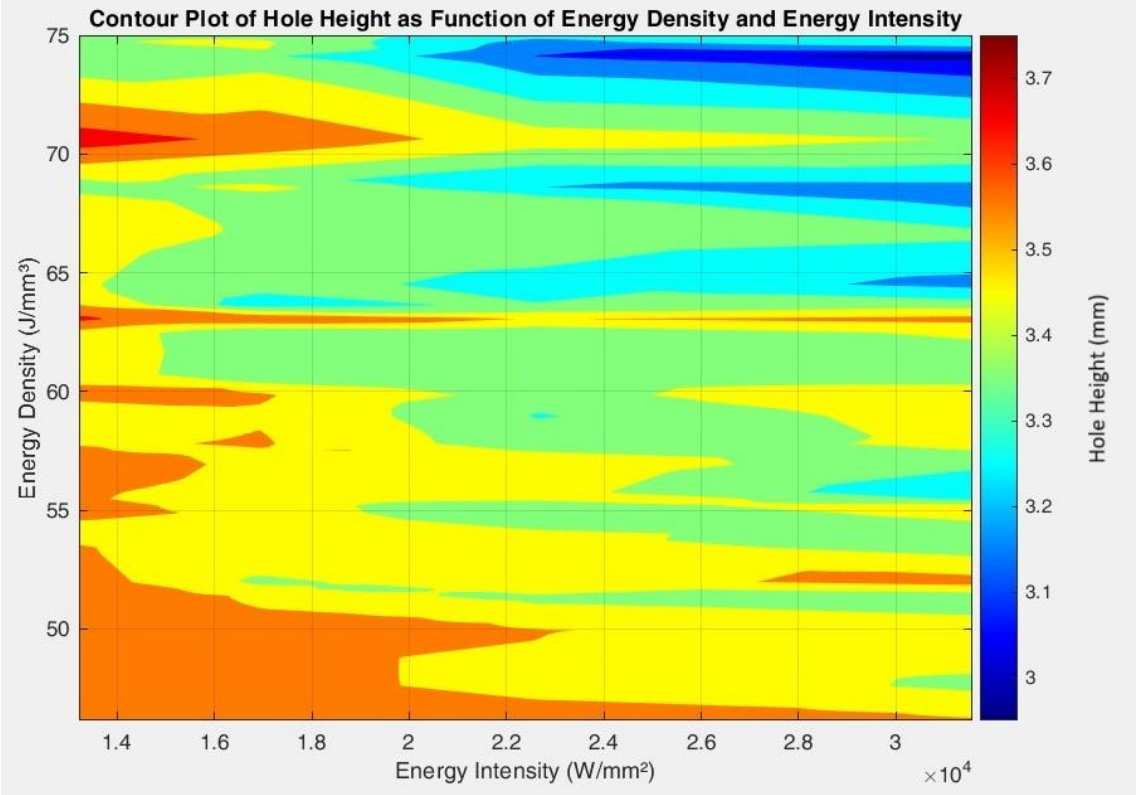


Figure 51 - Contour plot of hole height as function of Energy Density (J/mm³) and Energy Intensity (W/mm²)

This contour plot, which shows the results of the hole height as a function of all the printing parameters studied, supported by the two energy equations, corroborates the analyses made in the two previous graphs. In other words, the parts with the lowest energy intensity and energy density values (orange on the graph) have a better internal hole quality, i.e. with a height closer to the desired 4 mm. The regions that stand out the most are those corresponding to energy density ranges between 70-73 J/mm$^3$ and below 53 J/mm$^3$.

These horizontal regions on the graph indicates that the energy intensity has less influence on the size of the hole. Since the laser power is constant, the energy intensity only depends on the spot size parameter, so the spot size is not one of the most determining factors for dimensional accuracy. Therefore, energy density is the most important factor, so the key is to balance scanning speed and hatch spacing (since laser

power and layer height are constants) to achieve the right energy density, ensuring adequate melting without over-melting or under-melting. However, the hatch spacing parameter has a greater influence on the size of the internal hole when compared to the scanning speed, as can be seen in Figure 52. There is no direct relationship between scanning speed and hole size, only that the best results correspond to the lowest speed (500 mm/s). As the speed is lower, the laser stays longer in the same area, delivering more energy per unit length, which results in a more complete fusion of the powder, forming layers with better geometric definition.

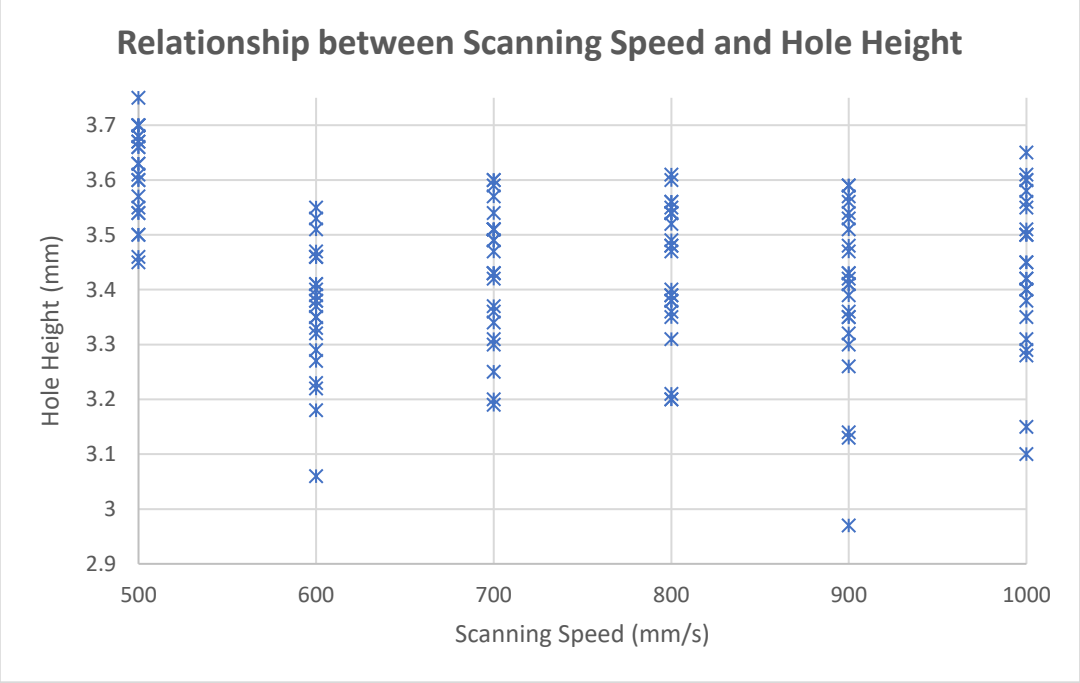


Figure 52 - Relationship between Scanning Speed and Hole Height

### 4.2.5 Roughness measurements

The results obtained from roughness measurements of the top face of the parts using the contact method are shown in Table 18.

Table 18 - Roughness results

| Part Number | Average Roughness (µm) | Standard Deviation (µm) |
|---|---|---|
| 76 | 18,93 | 2,91 |
| 137 | 20,11 | 1,88 |
| 121 | 27,1 | 2,98 |

Figure 53 shows the microscope images that were captured using the Olympus SZ-ET microscope at 12x magnification, from part 76, which has the lowest roughness values, to part 121, which has the highest roughness values.

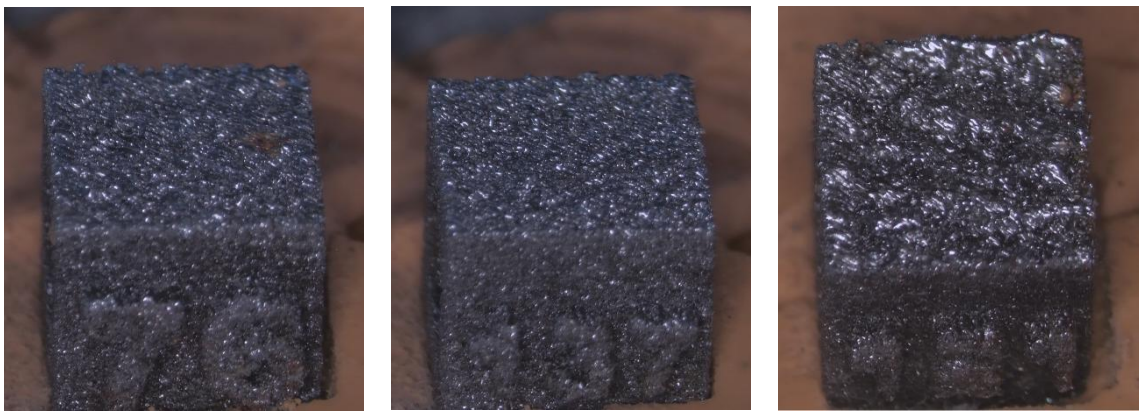

Figure 53 - Increasing roughness values, from left to right

Firstly, note that the roughness results are approximately 4x higher than those announced by the manufacturer (see table 9 general process data). This could be due to differences in printing conditions, from the printer or the different printing parameters selected, or even due to the dimensional differences found in the iron powder.

The surface roughness was greatly impacted by the printing parameters, as evidenced by the Ra values, which range from 18.93 µm (Part 76) to 27.1 µm (Part 121).

The standard deviations show the variability of roughness measurements for each part, ranging from 1.88 µm (Part 137) to 2.98 µm (Part 122). While Part 121 has the highest Ra and the most variability, which could be a sign of uneven melting or irregularities in the printing process, Part 137 has the most consistent surface (lowest standard deviation), indicating more uniform roughness across the measured areas.

Given that Part 76 has one of the smoothest surfaces and Part 121 has one of the roughest surfaces of all the parts in the sample, the results provide insight into the likely extreme roughness values for the entire batch of 144 parts. Based on the observed averages and deviations, the roughness range for the entire sample is estimated to be between 16 µm and 30 µm.

These conclusions could be improved with a larger data set, which would also help indicate the exact parameters that influence the smoother or rougher surfaces on all parts. However, the next subchapter evaluates the influence of each parameter on the roughness of the top face of the part by directly comparing the printed parts.

### 4.2.6 Influence of printing parameters on surface roughness

- **Hatch Spacing effect on roughness**

Figure 54 shows the evolution of surface roughness with increasing hatch spacing.

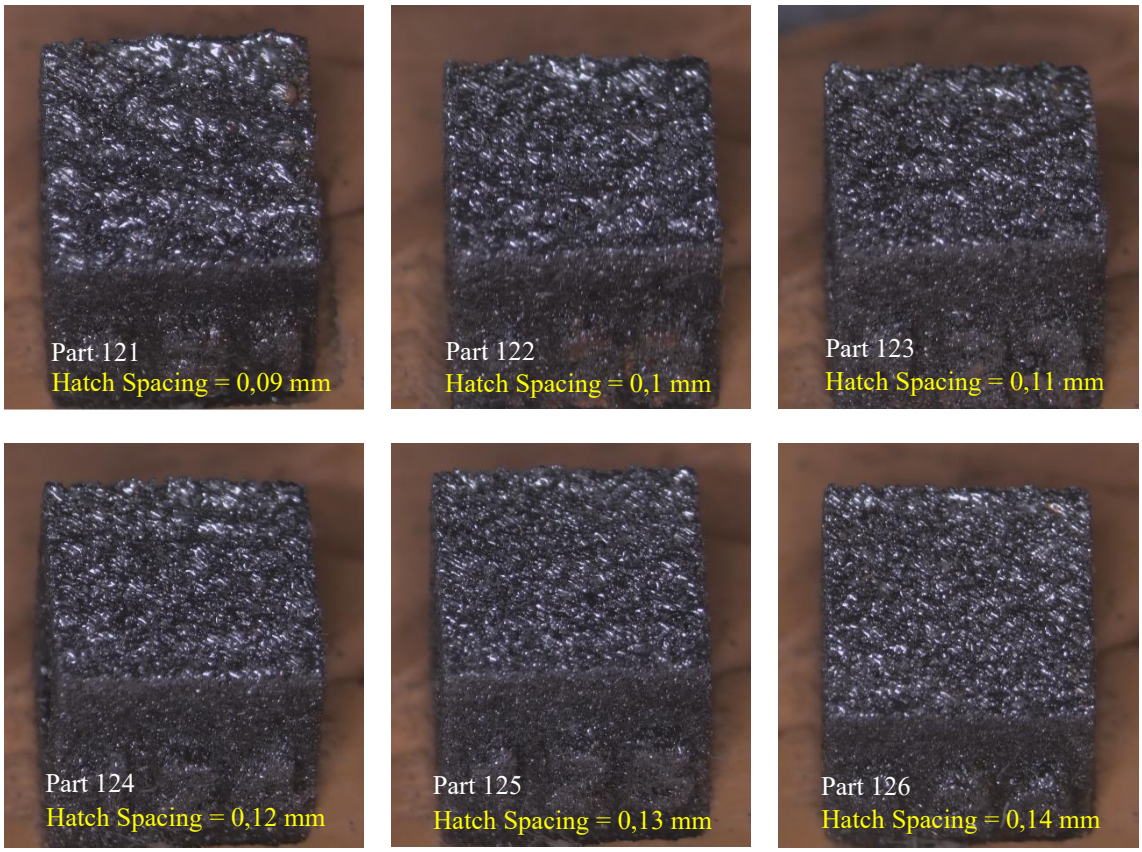


Figure 54 - Hatch spacing effect on cube´s upper face

An analysis of Figure 50 shows that the surface roughness improves as the hatch spacing increases. Comparing the pieces corresponding to the extreme values of hatch spacing, pieces 121 and 126, with hatch spacing of 0.09 and 0.14 mm respectively, it can be seen that piece 121 has a very uneven surface with several valleys and sharper peaks. These defects disappear over the course of the different images, until part number 126 is reached, which shows a much more uniform surface with fewer irregularities, where it is even possible to see the print direction lines perfectly (Figure 55).

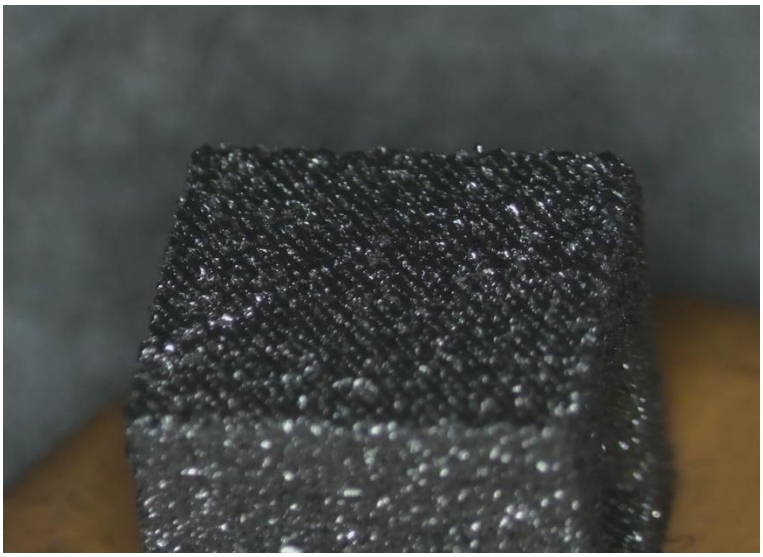

Figure 55 - Visible printing direction lines

These results can be explained by the fact that adjacent laser tracks overlap more when the hatch spacing is narrow. Due to this overlap, there is a higher local heat input, leading to higher likelihood of uneven melting or re-melting and greater surface roughness due to the creation of irregularities like spatter or balling [83]. On the other hand, if the hatch spacing is larger, adjacent laser tracks overlap less, generating lower localized heat input and more uniform cooling and solidification across the entire surface, resulting in a smoother top surface.

- **Scanning speed effect on roughness**

Figure 56 shows the evolution of surface roughness with increasing scanning speed.

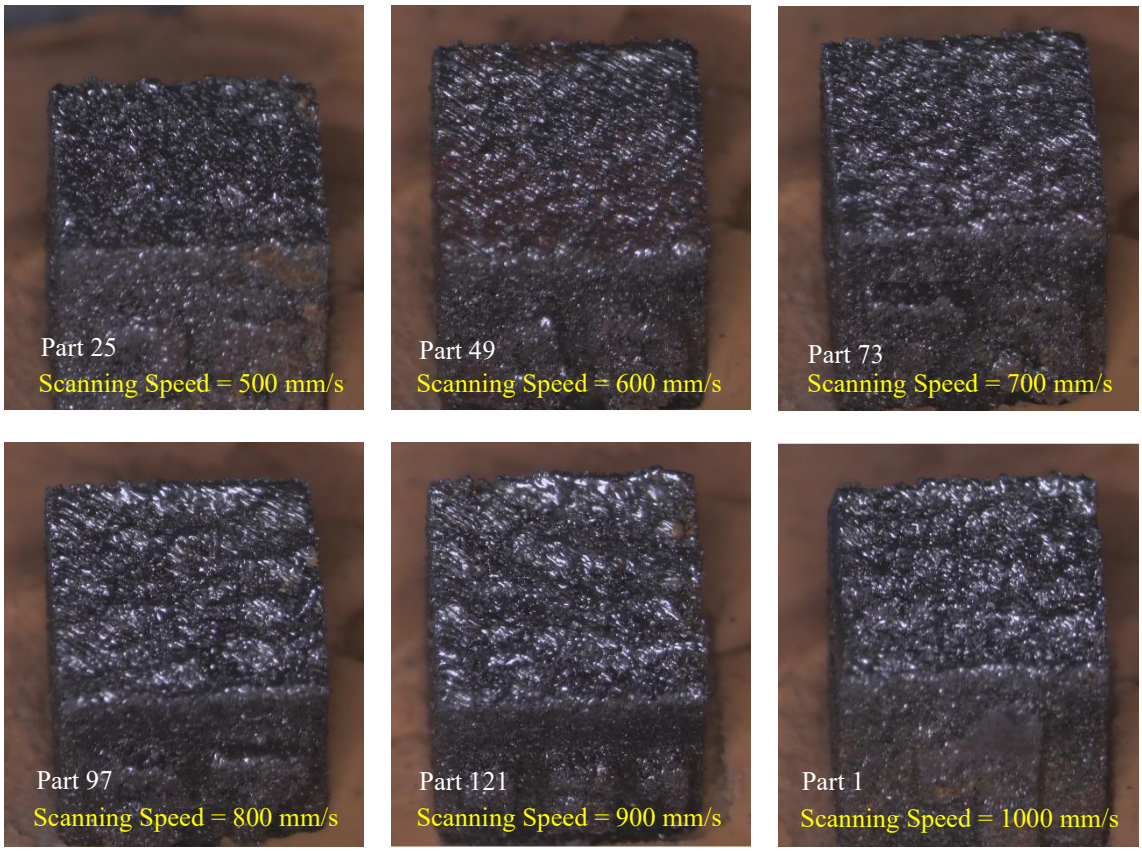


Figure 56 - Scanning speed effect on cube´s upper face

After observing Figure 51, it can be concluded that the parts with the best roughness are parts 25, 49 and 73, with scanning speed values of 500, 600 and 700 mm/s, respectively. Parts 97, 121 and 1, with scanning speed values of 800, 900 and 1000 mm/s, respectively, have much more irregular surfaces on the upper face and more pronounced roughness. It should be noted that as the scanning speed increases for these last three parts, these defects become more noticeable.

Since the laser moves more slowly at lower speeds (500–700 mm/s), the melt pool has more time to stabilize and smooth out irregularities. This results in a surface that is more uniform. When the laser travels too fast for the molten material to flow and settle uniformly, the melt pool shrinks and becomes less stable at higher speeds (800–1000

mm/s). This increase in speed can limit the size of the molten pool and the depth to which it penetrates, as well as the rate at which adjacent scanning tracks overlap, leading to valley defects and elevating Ra [89]. Rougher surfaces are the result of irregular solidification caused by increased turbulence triggered by this rapid motion.

It is important to note that for the energy density values to remain practically unchanged for all these parts as the scanning speed values increase, there has to be an adjustment in the hatch spacing values, i.e. to keep the energy density the same, the scanning speed and hatch spacing values have to be inversely proportional (see equation (1)), as one increases, the other has to decrease. This also proves the results observed in Figure 54, because from part 25 to part 1, the hatch spacing values decrease, which leads to an increase in roughness.

In conclusion, at lower speeds (500-700 mm/s), the melt pool remains stable, with enough time for the material to flow and solidify evenly [90], which means that to obtain good roughness on the top face, the optimum range for scanning speed would be around 500-700 mm/s. However, parts produced with 500 mm/s scanning speed showed more promising results.

- **Spot size effect on roughness**

Figure 57 shows the evolution of surface roughness with increasing spot size.

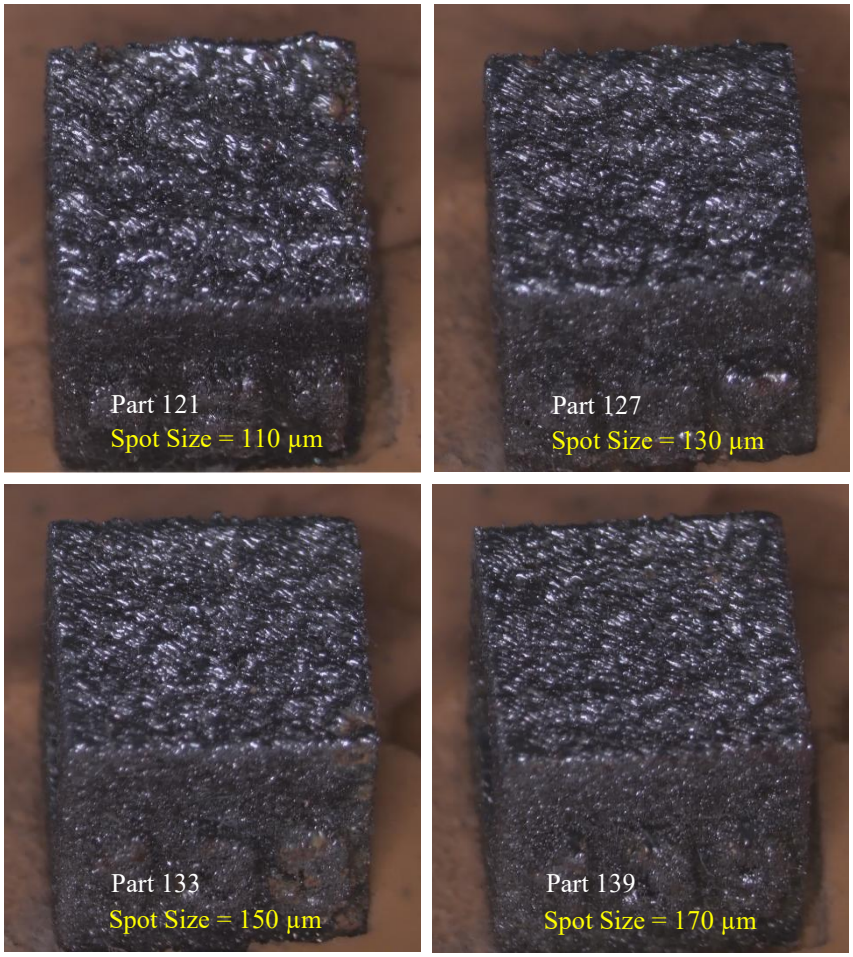


Figure 57 - Spot size effect on cube´s upper face

It can be seen that the roughness of the top face of the cubes improves as the spot size increases. This is especially noticeable when comparing the extreme results, piece number 121 with a spot size of 110 µm, which has a very uneven face, with piece number 139, with a spot size of 170 µm, where it is possible to see a much flatter and more uniform surface.

According to equation (2), which relates energy intensity to laser power and spot size, for lower spot size values (while maintaining the same laser power) the energy intensity will be higher, which could cause excessive melt pool agitation, balling effects, or localized overheating, resulting in rougher surfaces. On the other hand, the laser energy

is dispersed over a wider area with a larger laser spot size (lower energy intensity), creating a wider heat-affected zone, which allows the molten material to flow and settle evenly before solidification. As a result, there are fewer "spikes" in energy density or localized overheating, which can result in uneven melting and splattering.

Furthermore, greater spot sizes enhance scan track overlap, reducing uneven fusion and unfused particles that cause rough surfaces. Also, they reduce the prominence of loose particles by sintering more surrounding powder particles.

# 5. Conclusion and Future Perspectives

This thesis allowed the exploration of a broad and complex topic, such as 3D printing in the biomedical field. However, the extensive research carried out for this dissertation has provided a comprehensive perspective on various subjects, including bone composition, additive manufacturing, the Laser Powder Bed Fusion process and bone scaffolds. Based on this knowledge, it was possible to carry out a more complete and reliable analysis of the experimental results.

This work consisted of 2 main stages: firstly, the analysis of the used material, in which the iron powder was subjected to SEM and DLS analysis in order to obtain a morphological and dimensional characterization of the particles; the second stage consisted of evaluating 144 pieces of this printed material using the L-PBF process, in which the main objective was to study and analyze the influence of the printing parameters on the mechanical properties and effects on the geometry of the pieces. To this end, the factors studied were porosity, hardness, microstructure, the dimensional quality of the internal hole in the parts and the roughness of the top face of the parts. The results can be described as:

- After analysis of SEM images, the circularity and aspect ratio averages are around 0,62 and 2,03, respectively. These values shows that there is a large percentage of particles that are more irregular in shape, i.e. further away from a perfect sphere, typical from water atomized method;
- DLS revealed that the powder particles have approximately 2.5x the size of the ones presented in manufacturer data;
- The porosity study shows that the best results, i.e. the parts with the least porosity (density equal to or greater than 99%) correspond to those whose energy density is between 51-54 J/mm$^3$ and 58-63 J/mm$^3$. The parameter with the greatest influence was scanning speed, where the best results correspond to parts whose values are between 600-800 mm/s;
- The parts had an average hardness of 149 HV, which are promising results, since the part needs to have considerable hardness so that the implant doesn't suffer from premature corrosion or mechanical failure. The best results correspond to parts printed with lower energy densities (45-59 J/mm$^3$). Given that the most

important properties when printing these potential bone implants are their density and hardness, it is clear that the energy density ranges 51-54 J/mm$^3$ and 58-63 J/mm$^3$ are the ones to focus on.

- The microstructure of the printed parts is not homogeneous; grain sizes vary considerably. Furthermore, there is no discernible transition between successive printing layers;
- The dimensional accuracy of the inner hole showed the best results, i.e. the least accumulation of dust, for parts with energy densities between 70-73 J/mm3 and below 53 J/mm3. The printing parameter with the greatest impact on hole height was hatch spacing, with the height approaching the desired value as hatch spacing increased.
- Regarding the roughness of the upper face of the parts, it was found that this decreases with increasing hatch spacing; it increases with increasing scanning speed and decreases with increasing spot size.
- Overall, it was found that energy density was a determining factor in obtaining good results, unlike energy intensity, which did not have a strong influence. This leads to the conclusion that the spot size parameter may be the one that has the least direct impact on the mechanical properties of the parts and their changes in geometry.

It would be of great interest to have the opportunity to analyze the roughness of all the printed parts, as this would provide values for a large sample and the results would be more reliable. The main aim of the project, which will certainly remain the same, is to continue optimizing the printing parameters in order to obtain parts with the desired mechanical properties for this biomedical field, essentially high-density parts with sufficient hardness to withstand wear and tear. In addition, the design of the parts must always progress in order to obtain the desired cellular structures in the future.

This subject has many topics that were not covered experimentally during this dissertation, but it would be very interesting to study them in the future, such as in-depth research into the biocompatibility of pure iron with the human body and its resistance to corrosion.

## References


[1] Koons GL, Diba M, Mikos AG. Materials design for bone-tissue engineering. Nat Rev Mater 2020;5. https://doi.org/10.1038/s41578-020-0204-2.

[2] Einhorn TA. Clinically applied models of bone regeneration in tissue engineering research. Clin Orthop Relat Res, vol. 367, 1999. https://doi.org/10.1097/00003086-199910001-00007.

[3] Nazarzadeh Zare E, Mansour Lakouraj M, Mohseni M. Biodegradable polypyrrole/dextrin conductive nanocomposite: Synthesis, characterization, antioxidant and antibacterial activity. Synth Met 2014;187. https://doi.org/10.1016/j.synthmet.2013.09.045.

[4] Chaya A, Yoshizawa S, Verdelis K, Myers N, Costello BJ, Chou DT, et al. In vivo study of magnesium plate and screw degradation and bone fracture healing. Acta Biomater 2015;18. https://doi.org/10.1016/j.actbio.2015.02.010.

[5] Wegener B, Sievers B, Utzschneider S, Müller P, Jansson V, Rößler S, et al. Microstructure, cytotoxicity and corrosion of powder-metallurgical iron alloys for biodegradable bone replacement materials. Materials Science and Engineering: B, vol. 176, 2011. https://doi.org/10.1016/j.mseb.2011.04.017.

[6] Tapiero H, Tew KD. Trace elements in human physiology and pathology: Zinc and metallothioneins. Biomedicine and Pharmacotherapy 2003;57. https://doi.org/10.1016/S0753-3322(03)00081-7.

[7] Gao C, Feng P, Peng S, Shuai C. Carbon nanotube, graphene and boron nitride nanotube reinforced bioactive ceramics for bone repair. Acta Biomater 2017;61. https://doi.org/10.1016/j.actbio.2017.05.020.

[8] Carluccio D, Demir AG, Bermingham MJ, Dargusch MS. Challenges and Opportunities in the Selective Laser Melting of Biodegradable Metals for Load-Bearing Bone Scaffold Applications. Metall Mater Trans A Phys Metall Mater Sci 2020;51. https://doi.org/10.1007/s11661-020-05796-z.

[9] Bhardwaj A, Pandey LM. Biomaterials: Types and Applications. Nanoscale Engineering of Biomaterials: Properties and Applications, 2022. https://doi.org/10.1007/978-981-16-3667-7_4.

[10] Liu Y, Luo D, Wang T. Hierarchical Structures of Bone and Bioinspired Bone Tissue Engineering. Small 2016;12. https://doi.org/10.1002/smll.201600626.

[11] Walsh JS. Normal bone physiology, remodelling and its hormonal regulation. Surgery (United Kingdom) 2015;33. https://doi.org/10.1016/j.mpsur.2014.10.010.

[12] Piaia L, Salmoria G V., Hotza D. Additive manufacturing of nanostructured bone scaffolds. Nanostructured Biomaterials for Cranio-Maxillofacial and Oral Applications, 2018. https://doi.org/10.1016/B978-0-12-814621-7.00010-X.

[13] Souza JCM, Hotza D, Henriques B, Boccaccini AR. Nanostructured biomaterials for cranio-maxillofacial and oral applications. 2018. https://doi.org/10.1016/C2017-0-01060-1.

[14] Piccinini M. Prediction of peri-implant bone adaptation to mechanical environments: theoretical developments and experimental validation. 2014.

[15] University of Cambridge. Dissemination of IT for the Promotion of Materials Science (DoITPoMS): Mechanical properties of bone n.d.

[16] Anvari A. Characterization of Implantation's Biomaterials Based on the Patient and Doctor Expectations. Research in Medical & Engineering Sciences 2018;4. https://doi.org/10.31031/rmes.2018.04.000583.

[17] Henkel J, Woodruff MA, Epari DR, Steck R, Glatt V, DIckinson IC, et al. Bone Regeneration Based on Tissue Engineering Conceptions-A 21st Century Perspective. Bone Res 2013;1. https://doi.org/10.4248/BR201303002.

[18] Yu X, Tang X, Gohil S V., Laurencin CT. Biomaterials for Bone Regenerative Engineering. Adv Healthc Mater 2015;4. https://doi.org/10.1002/adhm.201400760.

[19] Pearlin, Nayak S, Manivasagam G, Sen D. Progress of Regenerative Therapy in Orthopedics. Curr Osteoporos Rep 2018;16. https://doi.org/10.1007/s11914-018-0428-x.

[20] Karageorgiou V, Kaplan D. Porosity of 3D biomaterial scaffolds and osteogenesis. Biomaterials 2005;26. https://doi.org/10.1016/j.biomaterials.2005.02.002.

[21] Zhang Y, Sun N, Zhu M, Qiu Q, Zhao P, Zheng C, et al. The contribution of pore size and porosity of 3D printed porous titanium scaffolds to osteogenesis. Biomaterials Advances 2022;133. https://doi.org/10.1016/j.msec.2022.112651.

[22] Jiao J, Hong Q, Zhang D, Wang M, Tang H, Yang J, et al. Influence of porosity on osteogenesis, bone growth and osteointegration in trabecular tantalum scaffolds fabricated by additive manufacturing. Front Bioeng Biotechnol 2023;11. https://doi.org/10.3389/fbioe.2023.1117954.

[23] Helou M, Kara S. Design, analysis and manufacturing of lattice structures: An overview. Int J Comput Integr Manuf 2018;31. https://doi.org/10.1080/0951192X.2017.1407456.

[24] Tao W, Leu MC. Design of lattice structure for additive manufacturing. International Symposium on Flexible Automation, ISFA 2016, 2016. https://doi.org/10.1109/ISFA.2016.7790182.

[25] Mahmoud D, Elbestawi MA. Lattice structures and functionally graded materials applications in additive manufacturing of orthopedic implants: A review. Journal of Manufacturing and Materials Processing 2017;1. https://doi.org/10.3390/jmmp1020013.

[26] Park KM, Min KS, Roh YS. Design Optimization of Lattice Structures under Compression: Study of Unit Cell Types and Cell Arrangements. Materials 2022;15. https://doi.org/10.3390/ma15010097.

[27] Riva L, Ginestra PS, Ceretti E. Mechanical characterization and properties of laser-based powder bed–fused lattice structures: a review. International Journal of Advanced Manufacturing Technology 2021;113. https://doi.org/10.1007/s00170-021-06631-4.

[28] Sagbas B, Gurkan D. Additively manufactured Ti6Al4V lattice structures for biomedical applications. International Journal of 3D Printing Technologies and Digital Industry 2021;5. https://doi.org/10.46519/ij3dptdi.953315.

[29] Sefene EM. State-of-the-art of selective laser melting process: A comprehensive review. J Manuf Syst 2022;63. https://doi.org/10.1016/j.jmsy.2022.04.002.

[30] O'Brien FJ. Biomaterials & scaffolds for tissue engineering. Materials Today 2011;14. https://doi.org/10.1016/S1369-7021(11)70058-X.

[31] Alaribe FN, Manoto SL, Motaung SCKM. Scaffolds from biomaterials: Advantages and limitations in bone and tissue engineering. Biologia (Bratisl) 2016;71. https://doi.org/10.1515/biolog-2016-0056.

[32] Moritz T, Maleksaeedi S. Additive manufacturing of ceramic components. Additive Manufacturing: Materials, Processes, Quantifications and Applications, 2018. https://doi.org/10.1016/B978-0-12-812155-9.00004-9.

[33] Baino F. Bioactive glasses – When glass science and technology meet regenerative medicine. Ceram Int 2018;44. https://doi.org/10.1016/j.ceramint.2018.05.180.

[34] Bratton EM, Durairaj VD. Orbital implants for fracture repair. Curr Opin Ophthalmol 2011;22. https://doi.org/10.1097/ICU.0b013e3283499409.

[35] Sell SA, Wolfe PS, Garg K, McCool JM, Rodriguez IA, Bowlin GL. The use of natural polymers in tissue engineering: A focus on electrospun extracellular matrix analogues. Polymers 2010;2. https://doi.org/10.3390/polym2040522.

[36] Gunatillake P, Mayadunne R, Adhikari R. Recent developments in biodegradable synthetic polymers. Biotechnol Annu Rev 2006;12. https://doi.org/10.1016/S1387-2656(06)12009-8.

[37] Schicker M, Seitz H, Drosse I, Seitz S, Mutschler W. Biomaterials as scaffold for bone tissue engineering. European Journal of Trauma 2006;32. https://doi.org/10.1007/s00068-006-6047-8.

[38] Ligon SC, Liska R, Stampfl J, Gurr M, Mülhaupt R. Polymers for 3D Printing and Customized Additive Manufacturing. Chem Rev 2017;117. https://doi.org/10.1021/acs.chemrev.7b00074.

[39] Nagels J, Stokdijk M, Rozing PM. Stress shielding and bone resorption in shoulder arthroplasty. J Shoulder Elbow Surg 2003;12. https://doi.org/10.1067/mse.2003.22.

[40] Manivasagam G, Dhinasekaran D, Rajamanickam A. Biomedical Implants: Corrosion and its Prevention - A Review. Recent Patents on Corrosion Science 2010;2. https://doi.org/10.2174/1877610801002010040.

[41] Liu Y, Zheng Y, Chen XH, Yang JA, Pan H, Chen D, et al. Fundamental Theory of Biodegradable Metals—Definition, Criteria, and Design. Adv Funct Mater 2019;29. https://doi.org/10.1002/adfm.201805402.

[42] Qu H, Fu H, Han Z, Sun Y. Biomaterials for bone tissue engineering scaffolds: A review. RSC Adv 2019;9. https://doi.org/10.1039/c9ra05214c.

[43] Shuai C, Li S, Peng S, Feng P, Lai Y, Gao C. Biodegradable metallic bone implants. Mater Chem Front 2019;3. https://doi.org/10.1039/c8qm00507a.

[44] Papanikolaou G, Pantopoulos K. Iron metabolism and toxicity. Toxicol Appl Pharmacol 2005;202. https://doi.org/10.1016/j.taap.2004.06.021.

[45] Cladera A, Weber B, Leinenbach C, Czaderski C, Shahverdi M, Motavalli M. Iron-based shape memory alloys for civil engineering structures: An overview. Constr Build Mater 2014;63. https://doi.org/10.1016/j.conbuildmat.2014.04.032.

[46] Ibtisam A. Biodegradable Metallic Materials: Revolutionizing Medical Implants and Devices 2024.

[47] Mostaed E, Sikora-Jasinska M, Drelich JW, Vedani M. Zinc-based alloys for degradable vascular stent applications. Acta Biomater 2018;71. https://doi.org/10.1016/j.actbio.2018.03.005.

[48] Liang W, Zhou C, Zhang H, Bai J, Jiang B, Jiang C, et al. Recent advances in 3D printing of biodegradable metals for orthopaedic applications. J Biol Eng 2023;17. https://doi.org/10.1186/s13036-023-00371-7.

[49] Wolf FI, Cittadini A. Chemistry and biochemistry of magnesium. Mol Aspects Med 2003;24. https://doi.org/10.1016/S0098-2997(02)00087-0.

[50] Hartwig A. Role of magnesium in genomic stability. Mutation Research - Fundamental and Molecular Mechanisms of Mutagenesis 2001;475. https://doi.org/10.1016/S0027-5107(01)00074-4.

[51] Tang HP, Qian M, Liu N, Zhang XZ, Yang GY, Wang J. Effect of Powder Reuse Times on Additive Manufacturing of Ti-6Al-4V by Selective Electron Beam Melting. JOM 2015;67. https://doi.org/10.1007/s11837-015-1300-4.

[52] Hebert RJ. Viewpoint: metallurgical aspects of powder bed metal additive manufacturing. J Mater Sci 2016;51. https://doi.org/10.1007/s10853-015-9479-x.

[53] Dawes J, Bowerman R, Trepleton R. Introduction to the additive manufacturing powder metallurgy supply chain. Johnson Matthey Technology Review 2015;59. https://doi.org/10.1595/205651315X688686.

[54] Popovich A, Sufiiarov V. Metal Powder Additive Manufacturing. New Trends in 3D Printing, InTech; 2016. https://doi.org/10.5772/63337.

[55] Torrent CJJ, Sajadifar SV, Gerstein G, Richter J, Niendorf T. Influence of Various Processing Routes in Additive Manufacturing on Microstructure and Monotonic Properties of Pure Iron—A Review-like Study. Metals (Basel) 2024;14. https://doi.org/10.3390/met14050557.

[56] Herzog D, Seyda V, Wycisk E, Emmelmann C. Additive manufacturing of metals. Acta Mater 2016;117. https://doi.org/10.1016/j.actamat.2016.07.019.

[57] Kabir SMF, Mathur K, Seyam AFM. A critical review on 3D printed continuous fiber-reinforced composites: History, mechanism, materials and properties. Compos Struct 2020;232. https://doi.org/10.1016/j.compstruct.2019.111476.

[58] Solomon IJ, Sevvel P, Gunasekaran J. A review on the various processing parameters in FDM. Mater Today Proc, vol. 37, 2020. https://doi.org/10.1016/j.matpr.2020.05.484.

[59] Kanishka K, Acherjee B. Revolutionizing manufacturing: A comprehensive overview of additive manufacturing processes, materials, developments, and challenges. J Manuf Process 2023;107. https://doi.org/10.1016/j.jmapro.2023.10.024.

[60] ASTM/ISO 52900. Additive Manufacturing - General Principles - Terminology. ASTM International 2021;2021.

[61] Zhai X, Jin L, Jiang J. A survey of additive manufacturing reviews. Materials Science in Additive Manufacturing 2022;1. https://doi.org/10.18063/msam.v1i4.21.

[62] Kruth J, Vandenbroucke B, Vaerenbergh J, Mercelis P. Benchmarking of different SLS/SLM processes as rapid manufacturing techniques. Int. Conf. Polymers & Moulds Innovations (PMI), Gent, Belgium, April 20-23, 2005, 2005.

[63] Yasa E. CT, KJP. "Selective Laser Sintering/Melting and Selective Laser Erosion with Nd:YAG Lasers," In Advances in Laser and Optics Research . Hauppauge NY: Nova Publishers 2012:1–64.

[64] Ansari P, Rehman AU, Pitir F, Veziroglu S, Mishra YK, Aktas OC, et al. Selective laser melting of 316l austenitic stainless steel: Detailed process understanding using multiphysics simulation and experimentation. Metals (Basel) 2021;11. https://doi.org/10.3390/met11071076.

[65] Schmidt M, Merklein M, Bourell D, Dimitrov D, Hausotte T, Wegener K, et al. Laser based additive manufacturing in industry and academia. CIRP Annals 2017;66. https://doi.org/10.1016/j.cirp.2017.05.011.

[66] Yasa E. Selective laser melting: Principles and surface quality. Addit Manuf, 2021. https://doi.org/10.1016/B978-0-12-818411-0.00017-3.

[67] Fukuda A, Takemoto M, Saito T, Fujibayashi S, Neo M, Pattanayak DK, et al. Osteoinduction of porous Ti implants with a channel structure fabricated by selective laser melting. Acta Biomater 2011;7. https://doi.org/10.1016/j.actbio.2011.01.037.

[68] Wehmöller M, Warnke PH, Zilian C, Eufinger H. Implant design and production-a new approach by selective laser melting. Int Congr Ser 2005;1281. https://doi.org/10.1016/j.ics.2005.03.155.

[69] Sing SL, Huang S, Goh GD, Goh GL, Tey CF, Tan JHK, et al. Emerging metallic systems for additive manufacturing: In-situ alloying and multi-metal processing in laser powder bed fusion. Prog Mater Sci 2021;119. https://doi.org/10.1016/j.pmatsci.2021.100795.

[70] Gibson I, Rosen D, Stucker B. Additive manufacturing technologies: 3D printing, rapid prototyping, and direct digital manufacturing, second edition. 2015. https://doi.org/10.1007/978-1-4939-2113-3.

[71] Aboulkhair NT, Everitt NM, Ashcroft I, Tuck C. Reducing porosity in AlSi10Mg parts processed by selective laser melting. Addit Manuf 2014;1. https://doi.org/10.1016/j.addma.2014.08.001.

[72] Yap CY, Chua CK, Dong ZL, Liu ZH, Zhang DQ, Loh LE, et al. Review of selective laser melting: Materials and applications. Appl Phys Rev 2015;2. https://doi.org/10.1063/1.4935926.

[73] Zhang B, Li Y, Bai Q. Defect Formation Mechanisms in Selective Laser Melting: A Review. Chinese Journal of Mechanical Engineering (English Edition) 2017;30. https://doi.org/10.1007/s10033-017-0121-5.

[74] Chowdhury S, Yadaiah N, Prakash C, Ramakrishna S, Dixit S, Gupta LR, et al. Laser powder bed fusion: a state-of-the-art review of the technology, materials, properties & defects, and numerical modelling. Journal of Materials Research and Technology 2022;20. https://doi.org/10.1016/j.jmrt.2022.07.121.

[75] Liu J, Wei B, Chang H, Li J, Yang G. Review of Visual Measurement Methods for Metal Vaporization Processes in Laser Powder Bed Fusion. Micromachines (Basel) 2023;14. https://doi.org/10.3390/mi14071351.

[76] Gu D, Shen Y. Processing conditions and microstructural features of porous 316L stainless steel components by DMLS. Appl Surf Sci 2008;255. https://doi.org/10.1016/j.apsusc.2008.06.118.

[77] DebRoy T, Wei HL, Zuback JS, Mukherjee T, Elmer JW, Milewski JO, et al. Additive manufacturing of metallic components – Process, structure and properties. Prog Mater Sci 2018;92. https://doi.org/10.1016/j.pmatsci.2017.10.001.

[78] Wang D, Yang Y, Liu R, Xiao D, Sun J. Study on the designing rules and processability of porous structure based on selective laser melting (SLM). J Mater Process Technol 2013;213. https://doi.org/10.1016/j.jmatprotec.2013.05.001.

[79] Strano G, Hao L, Everson RM, Evans KE. Surface roughness analysis, modelling and prediction in selective laser melting. J Mater Process Technol 2013;213. https://doi.org/10.1016/j.jmatprotec.2012.11.011.

[80] https://www.colibriumadditive.com/sites/default/files/41222_DMLM_M2Series5_Bro_4_US_EN_v1d%20%282%29.pdf n.d.

[81] https://www.thermofisher.com/pt/en/home/electron-microscopy/products/desktop-scanning-electron-microscopes/phenom-xl.html n.d.

[82] https://qmp-powders.com/wp-content/uploads/ATOMET_FeAM.pdf

[83] Nandhakumar R, Venkatesan K. A process parameters review on selective laser melting-based additive manufacturing of single and multi-material: Microstructure, physical properties, tribological, and surface roughness. Mater Today Commun 2023;35. https://doi.org/10.1016/j.mtcomm.2023.105538.

[84] Palousek D, Pantelejev L, Zikmund T, Koutny D. Processing of nearly pure iron using 400W selective laser melting – Initial study. MM Science Journal 2017;2017. https://doi.org/10.17973/MMSJ.2017_02_2016184.

[85] Lejček P, Čapek J, Roudnická M, Molnárová O, Maňák J, Duchoň J, et al. Selective laser melting of iron: Multiscale characterization of mechanical properties. Materials Science and Engineering: A 2021;800. https://doi.org/10.1016/j.msea.2020.140316.

[86] 52900:2015 A. Standard Terminology for Additive Manufacturing – General Principles – Terminology. ASTM International 2015.

[87] Mutua J, Nakata S, Onda T, Chen ZC. Optimization of selective laser melting parameters and influence of post heat treatment on microstructure and mechanical properties of maraging steel. Mater Des 2018;139. https://doi.org/10.1016/j.matdes.2017.11.042.

[88] Khorasani AM, Gibson I, Awan US, Ghaderi A. The effect of SLM process parameters on density, hardness, tensile strength and surface quality of Ti-6Al-4V. Addit Manuf 2019;25. https://doi.org/10.1016/j.addma.2018.09.002.

[89] Zhang H, Xu M, Liu Z, Li C, Kumar P, Liu Z, et al. Microstructure, surface quality, residual stress, fatigue behavior and damage mechanisms of selective laser melted 304L stainless steel considering building direction. Addit Manuf 2021;46. https://doi.org/10.1016/j.addma.2021.102147.

[90] Jażdżewska M, Kwidzińska DB, Seyda W, Fydrych D, Zieliński A. Mechanical properties and residual stress measurements of grade IV titanium and Ti-6Al-4V and Ti-13Nb-13Zr titanium alloys after laser treatment. Materials 2021;14. https://doi.org/10.3390/ma14216316.